Med-X (2023) 1:4
https://doi.org/10.1007/s44258-023-00003-1

Med-X

REVIEW

MRI-guided robot intervention—current state-of-the-art and new challenges

Shaoping Huang[1,2] · Chuqian Lou[1,3] · Ying Zhou[4] · Zhao He[1,2] · Xuejun Jin[1,4] · Yuan Feng[1,2] · Anzhu Gao[5,6] · Guang-Zhong Yang[1,2]

Received: 24 February 2023 / Revised: 14 March 2023 / Accepted: 15 March 2023

Abstract

Magnetic Resonance Imaging (MRI) is now a widely used modality for providing multimodal, high-quality soft tissue contrast images with good spatiotemporal resolution but without subjecting patients to ionizing radiation. In addition to its diagnostic potential, its future theranostic value lies in its ability to provide MRI-guided robot intervention with combined structural and functional mapping, as well as integrated instrument localization, target recognition, and in situ, in vivo monitoring of the therapeutic efficacy. Areas of current applications include neurosurgery, breast biopsy, cardiovascular intervention, prostate biopsy and radiotherapy. Emerging applications in targeted drug delivery and MRI-guided chemoembolization are also being pursued. Whilst promising progress has been made in recent years, there are still significant basic science research and engineering challenges. This paper provides a comprehensive review of the current state-of-the-art in MRI-guided robot intervention and allied technologies in actuation, sensing, new materials, interventional instruments, and interactive/real-time MRI. Potential future research directions and new clinical developments are also discussed.

Highlights

- Analysis of the current and emerging MRI-guided robot intervention systems for different clinical specialties.
- Critical review of allied technologies including actuation, sensing, new materials, interventional instruments, and interactive/real-time MRI.
- Future road map of new research directions and engineering approaches for expanding the future clinical applications of MRI-guided robotic systems.

Keywords MRI-guided robot intervention · Actuation · Sensing · Materials · Interventional instruments · Interactive/real-time MRI

✉ Guang-Zhong Yang
gzyang@sjtu.edu.cn

[1] Institute of Medical Robotics and School of Biomedical Engineering, Shanghai Jiao Tong University, Shanghai 200240, China

[2] National Engineering Research Center of Advanced Magnetic Resonance Technologies for Diagnosis and Therapy (NERC-AMRT), Shanghai Jiao Tong University, Shanghai 200240, China

[3] Materials and Technology Center of Robotics, Empa, Dübendorf 8600, Switzerland

[4] State Key Lab of Metal Matrix Composites and School of Materials Science and Engineering, Shanghai Jiao Tong University, Shanghai 200240, China

[5] Institute of Medical Robotics and Department of Automation, Shanghai Jiao Tong University, Shanghai 200240, China

[6] The Key Laboratory of System Control and Information Processing, Ministry of Education, Shanghai 200240, China

Published online: 11 July 2023

Introduction

Imaging techniques, whether being used for preoperative planning, intraoperative guidance, or post-operative assessment, are playing increasingly important roles in modern surgery. Techniques such as Computed Tomography (CT), ultrasound, and X-ray fluoroscopy are routinely used in general surgical workflows, providing detailed anatomical information to ensure surgical accuracy, consistency, and repeatability [1]. These techniques, however, are limited due to either ionizing radiation or intrinsic spatiotemporal resolution. Their ability to assess functional information is also restricted. MRI, on the other hand, is a versatile imaging modality that circumvents many of these drawbacks [2]. In addition to excellent morphological details and tissue contrast that can be fine-tuned through tailored pulse sequence design, it provides detailed functional information, including quantitative flow measurement, micro-circulation, susceptibility mapping, perfusion, diffusion, tissue strain, strain rate, and elastography. It can also present molecular information and metabolite markers, such as choline-containing molecules (Cho), creatine (Cr), phosphocreatine (PCr), and N-acetyl aspartate (NAA), for assessing, for example, the central nervous system.

Parallel advances have also been made in MR hardware to allow for integrated diagnosis and therapy. Improvements in hardware design particularly through novel coil arrays combined with fast reconstruction techniques have made real-time MRI possible. New magnet and gradient coils are continuingly reshaping the outlook of emerging MRI systems towards large bore or open access systems. These have paved the way for integrating real-time MRI with robotics for MRI-guided surgery. Early attempts have included neurosurgery, prostate biopsy, breast biopsy, and cardiovascular intervention [3], and new advances are expected to be made in areas such as targeted drug delivery and MRI-guided chemoembolization. The purpose of this paper is to provide a comprehensive review of the current state-of-the-art in MRI-guided surgical robotics and allied technologies in actuation, sensing, new materials, interventional instruments, and interactive/real-time MRI, as well as to outline the existing challenges and future research directions.

Current state-of-the-art in MRI-guided robot intervention systems

The prospect of integrating robotics with MRI has been anticipated in the early years of MRI-guided intervention systems. Whilst MRI provides rich morphological and function information and is free from ionizing radiation, conventional solenoid magnet designs have made access to the patient during intervention difficult. The use of remotely controlled robot actuation has clear advantages. However, electromagnetic compatibility with the MR environment poses significant challenges. Considering the safety of devices used in the MR environment, the American Society for Testing and Materials (ASTM) F2503 classified interventional systems working in the MR environment into three categories [4]: *MR Safe*, *MR Conditional*, and *MR Unsafe*. *MR Safe* means an item that poses no known hazards resulting from exposure to any MR environment. MR safe instruments consist of materials that are non-conductive, non-metallic, and non-magnetic. The term "*MR Conditional*" is different from "*MR Compatible*" which is an obsolete definition that was first defined in 1997 in the FDA draft guidance document. *MR Conditional* refers to an item that has been demonstrated to be safe in the MR environment under specified conditions, including the static magnetic field, the time-varying gradient magnetic fields, and the radiofrequency fields. Finally, *MR Unsafe* refers to instruments or systems that are deemed to be unsafe to be used in the MR environment.

In recent years, a plethora of MR conditional/safe robots have been developed for brain [5], breast [6], prostate [7], artery [8], liver [9], spinal cord [10], and oral [11] interventions. Figure 1 provides an overview of the existing MRI-guided surgical robot systems for different clinical scenarios. To make the comparison of the existing technologies meaningful, we have focused on features including Degrees-of-Freedom (DoF), accuracy, Remote Center of Motion (RCM), integrated instruments sensing, and the ability to provide interactive/real-time MRI during procedures. Firstly, the accuracy and DoF of MRI-guided surgical robots are the most critical performance for clinical intervention. Precision surgery needs to ensure minimal access to trauma and iatrogenic injury, which are particularly important for neurointervention and tissue biopsy. Secondly, the intrinsic DoF of the robot during surgery affects the dexterous operation of the robot. MRI-guided surgical robots need to operate in restricted MRI environment and the end effector needs to avoid critical structures, *e.g.*, important cranial nerves and blood vessels for Deep Brain Stimulation (DBS). More DoFs are needed if the robot is to be used for MRI-guided endoluminal intervention, in order to follow narrow, tortuous pathways.

In Fig. 1, we summarized the currently published MRI-guided surgical robot systems from a total of 95 independent studies and commercial products with eight different categories, including brain, breast, prostate, artery, liver, spinal cord, MRI-guided Focused Ultrasound (MRgFUS), and others (see Supplementary Information -1). These systems have all been completed with system design, integration,

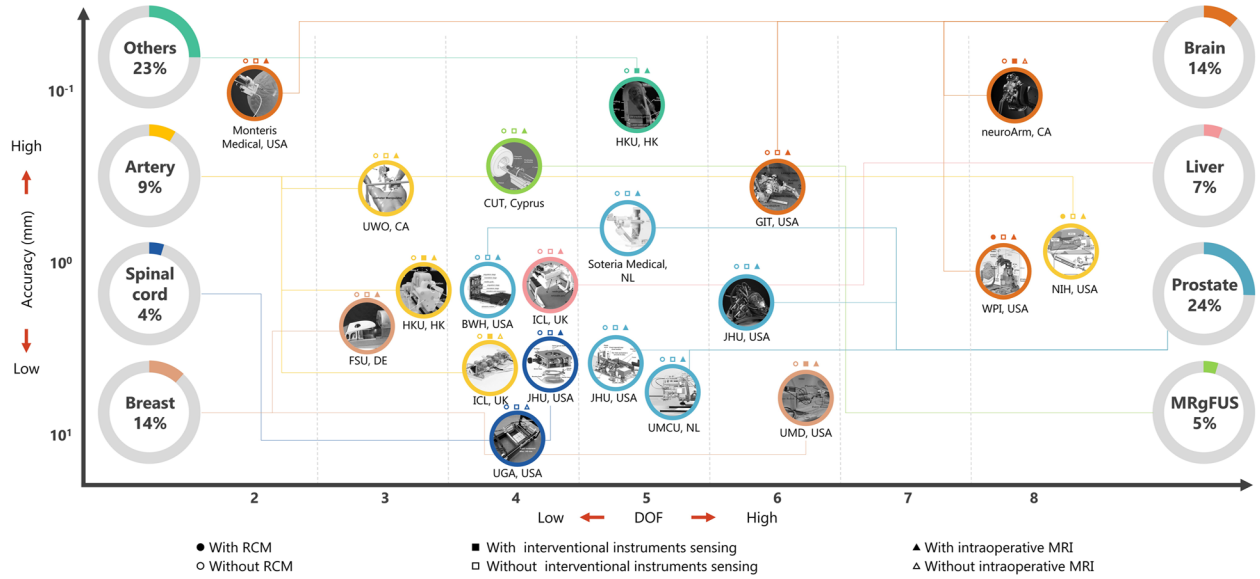

Fig. 1 A detailed analysis of the currently developed MRI-guided robot intervention systems in different clinical specialties. Twenty more advanced surgical robot systems are highlighted as individual icons, which are distributed by DoF (horizontal axis) and accuracy (vertical axis). The proportion of the number of MRI-guided robot intervention systems, based on 95 independent systems, in eight clinical specialties are shown on two sides of the figure. Out of the systems developed about 24% are for prostate surgery, mostly for biopsy [7, 12–15]; 14% are for brain surgery, typical applications including tumor removal [16], Laser Interstitial Thermo Therapy (LITT) [17], stereotaxic and microsurgery [5], DBS [18]; 14% for breast surgery, including biopsy [6, 19]; 9% for artery intervention, including Percutaneous Coronary Intervention (PCI) [8, 20, 21], electrophysiology [22], Transcatheter Aortic Valve Replacement (TAVR) [23]; 7% for liver surgery, application including laser ablation [9]; 5% for MRgFUS [24] and 4% for spinal cord surgery, including cannula alignment [10] and cellular therapeutics [25]

and validation in actual MR environments. Their application status may be at phantom (minimum requirement), ex vivo, cadaver, in vivo, or clinical validation with regulatory approval. For the same series of systems, we have only shown the most advanced version and the origin of the technical development can be found in relevant technical references. For example, we selected MINIR-II [16] for the MINIR series, which can be dated back to 2008 when the first result was published [26].

Figure 1 also shows the distribution of these 95 systems under the chosen eight categories. By excluding systems that have only conducted laboratory phantom experiments, twenty more advanced surgical robot systems are highlighted as individual icons in Fig. 1. These systems cover eight clinical specialties, including brain, artery, breast, prostate, liver, spinal cord, MRgFUS and others. For each robot, further information is provided regarding the country of origin, development team, and capabilities in terms of RCM, instrument sensing, and interactive MRI. RCM is a commonly used feature in robotics for adjusting the pose of the instruments passing through a fixed point in space, as determined, for example, by an incision point or a trocar in minimally invasive surgery. Instrument sensing mainly includes electrophysiological, temperature, force (direct contact force, torsional force), position, shape, and attitude sensing [27, 28]. Interactive perception and user feedback of the robot during operation are important for clinical deployment and integration with standard surgical workflows. Tactile or force sensing is important for providing perceptual feedback when instrument is interacting with different tissue or penetrating through different organs. Temperature sensing is important for controlling ablation power and mitigating the risk of overheating due to, for example, RF heating particularly for pulse sequences with high SAR (Specific Absorption Rate). Position sensing is important for closed-loop control for accurate targeting and motion adaptation during operation. For managing tortuous pathways and negotiating complex deformable or moving structures, optical-based 3D shape sensing is particularly useful for real-time instrument tracking and control. Other sensing modalities, such as vision and MR-based techniques, are used extensively, either independently or in combination.

From this survey, it has been found that in general, the accuracy and DoF of existing MRI-guided surgical robots for the brain are relatively high (mostly DoF > 5, accuracy < 1.5 mm) [5, 16, 18]. Although the NeuroBlate system is two DoF (translation and rotation) system, it requires a modified Navigus device to control the orientation of the system [17]. The accuracy of the currently used MRI-guided surgical robots for the prostate, on the other hand, is relatively low (accuracy > 2.5 mm) [7, 12–15], but the clinical experiments are relatively abundant (5 systems have already

undergone clinical validation and two have already gained FDA clearance). We will analyze in detail the key features involved in these systems later in this paper.

Key considerations of MR conditional/safe robots

Conventional areas of research in robotics include actuation, sensing, and control. For MRI-guided robotic intervention systems, the selection/ development of new materials, instrument design and imaging sequence development are also of particular importance. Additionally, it is necessary to strike a balance between operational performance and clinical requirements when addressing the need for accurate navigation and targeting. Key considerations of MR conditional/ safe robots include:

- Actuation and sensing – The core aspects of a robot are actuation and sensing. MRI-guided surgical robot systems need to rely on high precision sensing and stable actuation to achieve optimal performance with due consideration of MR safe/conditional operation conditions. This is an area that has attracted extensive research efforts in recent years [29, 30]. This review will discuss the basic principles of actuation and sensing in developing MRI-guided surgical robot systems and typical embodiments are also provided.
- Materials – The choice of materials dictates if the system is MR-safe or conditional. The ASTM Committee has a clear definition of medical devices in the MR environment [4]. Hitherto, limited studies have been carried out on MR conditional/safe materials [31]. In this paper, MR-conditional/safe materials are evaluated with a critical comparison of their relative performance and operational merit.
- Instrument design – A wide range of interventional devices or instruments have been developed and they are used for tissue ablation, DBS, biopsy, and catheterization. Some of these instruments have been successfully integrated with robotic systems and this review will provide a detailed analysis of typical interventional devices in use and some for the emerging platforms that are in development.
- Interactive/real-time MRI – To leverage the intrinsic advantages of MRI including superior soft-tissue contrast, simultaneous structural/functional mapping, metabolic profiling, and multi-plane imaging without ionizing radiation, MRI-guided robot intervention has the unique advantage of providing integrated diagnosis, therapy and post-operative assessment. The ability to provide interactive or real-time MRI is essential for providing closed-loop control or visual servoing for accurate targeting. This review will provide a detailed overview of existing as well as emerging MRI sequence designs and hardware improvements for rapid MRI.

Review organization and literature survey

The rest of this paper is to be organized as follows. In Sect. 2, we will first introduce actuation (Sect. 2.1) and sensing (Sect. 2.2), which are the foundation of an MR conditional robot. This is to be followed by MR conditional or safe materials used for robot components in Sect. 3. Existing and emerging interventional devices for MRI-guided intervention are presented in Sect. 4 and we subsequently discuss in Sect. 5 hardware development and new pulse sequence designs for interactive/real-time MRI. In Sect. 6, we will illustrate in detail eight exemplar surgical robot systems for different clinical specialties. Lastly, we will discuss the challenges and future outlook of MRI-guided surgical robots.

This review is based on a comprehensive literature search (up to January 2023) using databases including PubMed, Science Direct, Scopus, Web of Science, Bing, and patent databases (*e.g.*, Espacenet). The keywords used are in line with previous work [3, 29, 30, 32–36] for consistency, which covers five main categories: (a) robot system (mr/mri/magnetic resonance (imaging), guide, conditional/compatible/safe, robot, intervention/surgery), (b) actuation (mr/mri/magnetic resonance (imaging), conditional/compatible/safe, actuator/actuation/motor), (c) sensing (mr/mri/magnetic resonance (imaging), conditional/compatible/safe, sensing/sensor), (d) material (mr/mri/magnetic resonance (imaging), conditional/compatible/safe, biomaterial, metal/Ti alloy/Zr alloy/Cu alloy/ceramic/polymer, biocompatibility, magnetic susceptibility) (e) instrument (mr/mri/magnetic resonance (imaging), conditional/compatible/safe, electrode/catheter/ablation/interventional device/ablation/LITT/cryoablation/micro wave ablation/deep brain stimulation/biopsy/catheterization/guidewire/neurosurgery/injection) (f) MRI (mr/mri/magnetic resonance (imaging), real-time/intraoperative MRI-guided, intervention/surgery.

Actuation and sensing

Actuation

Traditional electric motors compose of permanent magnets and metals that are not MR safe. Furthermore, the electric motor can interfere with the reception of the imaging signals and affect field homogeneity of the region of interest (ROI), causing artifacts, distortion, signal loss or adding noise. In addition, the RF signal from MR imaging can generate eddy currents, affecting the performance of the electric motor.

Therefore, the main challenges of MR conditional actuators include material selection (metal, non-metallic, paramagnetic, etc.), working principle (pneumatic, hydraulic, electronic control, mechanical transmission), and signal shielding (RF signal, high strength magnetic field).

To address the above problems, four main strategies can be used: 1) replacing the metal parts with nonmetal components, *e.g.*, using pneumatic [37] or hydraulic [38] actuation; 2) introducing non-metallic, remote cable/shaft driven mechanism (*e.g.*, Kevlar cables) [39] for actuation; 3) adopting non-magnetic materials incorporating active shape deformation (*e.g.*, elastomer-based soft actuators [11], shape memory alloy (SMA)-based actuators [40]); 4) leveraging the magnetic field of the scanner, *e.g.*, using gradient magnetic field to actuate ferromagnetic bodies [41]. It is also possible to use the magnetic field generated by the superconducting magnet of the MRI itself to drive the servomotor [42]. Figure 2 summarizes the current MR conditional/safe actuators and hybrid actuators based on the above strategies. Table 1 shows the performance differences of presented actuators.

Pneumatic actuation

Pneumatic actuators are generally MR safe and they can use stable gas sources widely available in hospitals. The remote control can be realized by placing the actuator controller outside the scanner room. Airflow can be transmitted to the actuator through the tubes. The structure and material of the actuator can be modified for MR compatibility. A large number of MR conditional pneumatic motors have been developed [29], mainly following cylinder-based, gear-based, and blade-based designs.

a) Cylinder-based

This type of pneumatic actuator is similar to the conventional pneumatic actuator. The differences are in the usage of MR compatible materials, combined with MR conditional angle sensor, position sensor, or the way of step cycle action for realizing the rotation and linear movement of the motor. Pyrex® glass cylinder was used for Airport® with low friction and MR compatibility [62]. Yang et al. [52] developed a 1-DoF MR conditional pneumatically actuated robot for needle insertion. The system is pneumatically actuated using modified bidirectional cylinders (AC-13270–3, Airpot Corp., Norwalk, CT, USA). By using the optical encoder and the sliding-mode control strategy, the system has a position error of less than 1 mm. Melzer et al. [50] developed INNOMOTION for percutaneous interventions actuated by the pneumatic cylinder combined with a high-precision optical encoder. Chen et al. [51] developed a high-torque pneumatic stepper motor by using LEGO® pneumatic cylinders, cranks, and shafts. With a planetary gearbox, the step size is 3.6°, and the maximum output torque is 800 mNm.

b) Gear-based

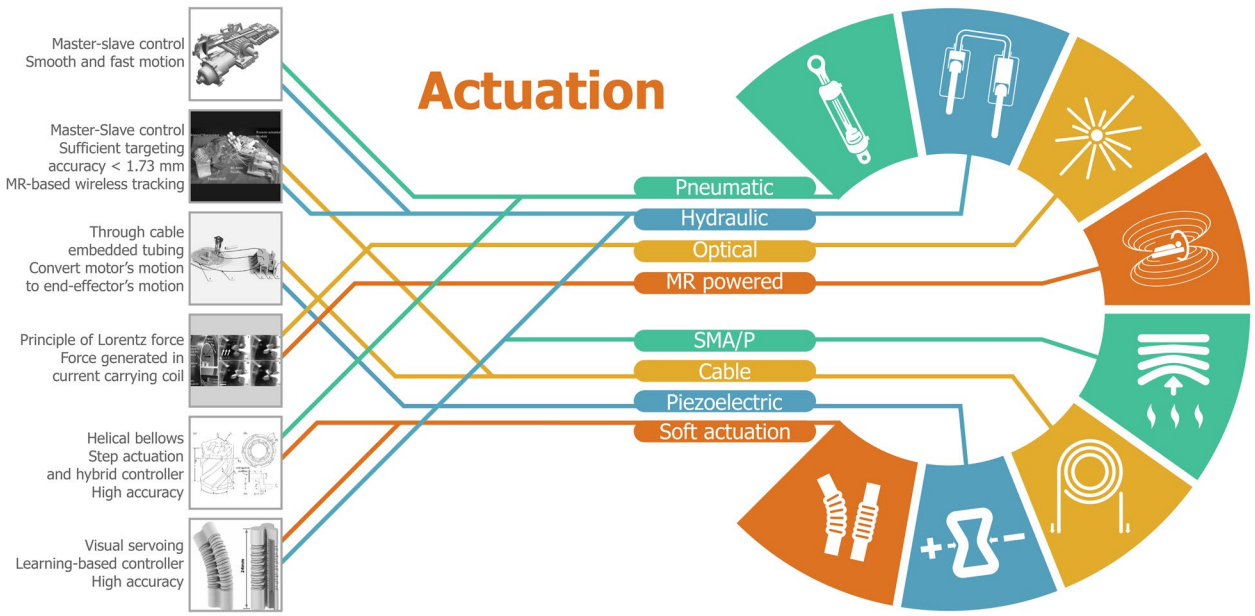

Fig. 2 Typical MR conditional/safe actuation methods for MRI-guided robotic intervention. Eight working principles include pneumatic (cylinder-based, gear-based, blade-based), hydraulic, soft actuators, piezoelectric, MR powered, SMA/P, optical, and cable. By combining these working principles, hybrid actuation schemes are also being pursued. These include: hydraulic/pneumatic [43], hydraulic/cable [44], piezoelectric/cable [39], MR powered/optical [45], pneumatic/soft actuators [46], and hydraulic/soft actuators [11]

Table 1 Typical actuation schemes for MR-safe/conditional robots

Actuation type	Methods	Size (mm)	Speed	Force/Torque	Accuracy/Resolution	SNR loss	Comments	Refs
Pneumatic	Gear-Based	Φ 85×35	180 rpm	0.6 Nm	3.3°	< 1%	Stable output Customized optical encoder	Stoianovici (2007) [37]
		25 ~ 80	300 mm/s 333 rpm	300 N 3.7 Nm	1 mm 10°	< 1%	Concise structure High force/torque output	Groenhuis (2018) [47, 48]
		90×90×90	800 rpm	0.39 Nm	2.25°	< 1%	Low cost Disposable	Farimani (2020) [49]
	Cylinder-based	NA	< 0.1 mm/s	395 N	1.5 mm	NA	High cost High accuracy	Melzer (2008) [50]
		95×60×35	< 14.4 °/s	800 mNm	3.6°	2.35%	High speed	Chen (2014) [51]
		Φ 19×152.4	NA	NA	1 mm	3.5%	Low friction Integrated force sensor	Yang (2011) [52]
	Blade-based	Φ 44×79	370 rpm	0.46 Nm	1.8°	< 5%	Continuous motion Customized optical encoder	Chen (2017) [53]
		Φ 68×25	2000 rpm	11 mNm	60°	NA	Less number of parts Easy to make	Liang (2022) [54]
Hydraulic	Rolling-diaphragm-sealed	150×140×46	2 Hz	0.49 Nm	0.64°	< 2%	High accuracy, Large size High torque output	Dong (2019) [38]
	Double rolling-diaphragm-sealed	Φ 30	0.86 Hz	> 30 N	0.5 mm	NA	High accuracy Large stroke length	Simonelli (2020) [55]
Soft actuator	Bellow	< 50	2.5 mm/s 0.83 rpm	0.06 Nm	0.5 mm 0.5°	< 1%	High accuracy Customized position controller	Comber (2016) [46]
	Inchworm	Φ 30×40	0.34 mm/s	2 N	1.1 mm	NA	Compact design Easy fabricate	Pfeil (2018) [56]
	Three chambers	Φ 12×100	2 mm/s	NA	0.2 mm	< 5%	High accuracy Small size	Fang (2021) [11]

Table 1 (continued)

Actuation type	Methods	Size (mm)	Speed	Force/Torque	Accuracy/Resolution	SNR loss	Comments	Refs
Piezoelectric	Modification of USR series piezo motor	30 ~ 60	250 rpm	630 Nmm	2.25°	6%	Modification needed to reduce SNR loss	Fischer (2008) [57]
	Modification of HR series piezo motor	10 ~ 50	250 mm/s	8N	1.27 mm	NA	MRI scanning process and surgical operation cannot work simultaneously	Krieger (2013) [58]
	Non-harmonic piezoelectric motors	25 ~ 100	27 mm/s	450N	NA	< 1%	High force or torque and moderate speed Not backdrivable Easier electric wave suppression	Su (2012) [59]
	Piezo-worm	50 × 50 × 30	9 mm/s	5 Nmm	NA	10%	Not backdrivable, linear and rotary motion	Eibannan (2012) [60]
MR powered	Magnetic field generated by MR scanner	Φ 50 × 100	1524 rpm	73.1 mNm	60°	1.5%	Latencies Poor controllability	Hofstetter (2022) [42]
SMA/P	Air/liquid-cooled for quick response	2.5 × 2.5 × 3.0	NA	1.5 N	5.5°	10%	Short stroke lengths High power-to-weight ratio, compact size and silent operation	Ho (2010) [40]
Optical	Photovoltaic cells embedded in the coil	NA	NA	100—200 μNm	NA	NA	Small torque Wireless actuation	Mutlu (2021) [45]
Cable	Torque transfer cable/tendon	NA	NA	94 N	NA	NA	Backdrivable Hysteresis and friction loss	Vigaru (2016) [61]

Gears or rack steps are commonly used designs for the pneumatic actuator. Because the step actuators do not require closed-loop control, it is of great interest for their use in the MR environment. Stoianovici et al. [37] developed the first gear-based pneumatic stepper motor. This motor was integrated into a custom fiber optical encoder and utilized in MRI-guided surgical systems [7]. Groenhuis et al. [47] developed a serial of stepper motors for linear or rotational motion with forces up to 330 N, torques up to 3.7 Nm, and a stepping frequency up to 320 Hz. The dimensions ranged from 25 to 80 mm, and the actuator was free of backlash and with power up to 26W. Farimani et al. [49] developed PneuAct-I and PneuAct-II, which had a scotch yoke mechanism to convert the linear motion into the rotation and a reduction drive for the desired function. The whole motor was 3D printed without any seals or bearings.

c) Blade-based

For blade-based pneumatic actuators, the gas acts on the rotor (blade) to rotate the shaft directly. This method can produce a large torque, but it needs exhausting air constantly and its energy efficiency is often limited. Because of continuous actuation, the motor relies on sensors to achieve closed-loop control. Chen et al. [53] developed a blade-based motor with a customized fiber-optical encoder that provided powerful and accurate actuation. It had two air inlets for motion and direction control and three outlets separated at 120°. Liang et al. [54] used a curtate hypocycloid rotor to achieve the step rotation. When the airflow blows to the side of the rotor, the rotor can be stabilized in a specific position because the special structure cooperates with the chamber.

Hydraulic actuators

Although both liquid actuation and pneumatic actuation are in similar driving modes, the transmission response time of liquid actuation is longer than that of gas drive due to viscous resistance. Thus, most pneumatic actuators for high-speed switching are not suitable for using liquid as an alternative medium. Although the liquid has high viscous resistance and low transmission response time, it can be used for high precision operation due to its incompressibility. The device of equivalent motion can be set at the master and slave sides to realize a master–slave motion design. By establishing the elastic model in the transmission process and detecting the liquid pressure of the pipeline, more accurate position control can be achieved.

In previous work, Dong et al. [38], for example, developed a high-performance continuous hydraulic motor with fast response (rise time < 40 ms), precise open-loop control of position (average error of 0.64°), and high output torque (0.49 Nm) using 10-m long hydraulic pipelines. Rolling-diaphragm-sealing was used for low friction piston movement and three cylinders were used for smooth rotary motion. Simonelli et al. [55] developed a double-acting diaphragm actuator with dual-piston heads. The experiment showed that the linear actuator exhibited less than 0.2 mm hysteresis (across 25 mm stroke length), and with high stiffness (10 kN/m), low transmission dead zone (3 N), and high accuracy (0.5 mm).

Soft actuators

Soft materials are often made of silicone, polydimethylsiloxane (PDMS), and other MR safe materials. Therefore, most of the current designs of soft robots are either MR safe or conditional [63]. Comber et al. [46] developed a bellow-based pneumatic actuator with helical and toroid-shaped bellows. It could provide rotation and translation because of the contraction and expansion of the bellow. A sliding mode controller with a substep control strategy was used for high accuracy control. The step size was 0.5 mm and 0.5° with steady-state errors of 0.013 mm and 0.018°. Pfeil et al. [56] designed a multi-material 3D print linear actuator based on the inchworm principle. Simplified modeling was introduced for this type of actuator synthesis. By using multi-material 3D printing, the actuator was integrated with rigid and flexible materials with good needle drive performance (a velocity of 0.34 mm/s with a 2 N load). Fang et al. [11] developed a hydraulic soft actuator with two segments—one segment was used for active bending and the other one was used for fine distal laser manipulating. Each segment comprised three elastomeric chambers actuated by fluidic inflation/deflation. A learning-based model was trained for high accuracy path-following ablation tasks (accuracy 0.2 mm).

Piezoelectric actuators

Piezoelectric actuators represent a mature MR conditional solution. They are favorable for MR conditional use due to their compact size. Piezoelectric motors rely on the geometric change of piezoelectric material to create motion under specific electric fields. It can be generally classified into two categories with harmonic or nonharmonic driving signals. Harmonic motors typically operate with high-voltage sinusoidal drive waveforms, whereas nonharmonic motors often have contact pads that push against a sliding surface using several lower-voltage arbitrary waveforms. A special piezo-worm actuator is also designed to combine multiple piezo stacks, achieving both linear and rotating motion. Piezoelectric motors have the advantage of accuracy, reliability and self-locking capability. None of the existing off-the-shelf piezo motors is defined as MR-safe, specially designed shielding and signal control may be needed to ensure the actuator is safe for use in the MR environment. Research

results indicated that less than three piezo actuators in the MR environment are acceptable. But the multi-DoF robots with these motors showed a significant signal to noise ratio (SNR) loss. Most of these motors are not specially designed for use in MR environments as most of them contain some metallic parts. Commercially available piezoelectric motors can cause up to 40%—80% SNR loss during synchronous robot motion. Some effort has been directed to replacing [57] and modifying them to minimize the electrical and magnetic artifacts.

MR powered actuation

MR scanners can magnetize and induce motion with ferromagnetic particles. This principle was used in [64] to induce a ferromagnetic spherical ball embedded in nonmetallic chassis and gears. MR scanner and nonmetallic chassis acted as a stator, and the rotor was a lever arm holding the ferromagnetic spherical ball. The magnetic field of the scanner generated forces in the ferromagnetic ball, and thus continuous rotor motion can be created. This MR powered actuator with open-loop control can generate a force of 0.76 N [64]. With further development, the MR image of the actuator was used for closed-loop control [65]. The motor had higher torque, velocity, and output force (9.4N), but significant latencies can be observed. Hofstetter et al. [42] developed an MR conditional electromagnetic servomotor combining the electromagnetic motor concept with a non-magnetic optical encoder to achieve closed-loop control. A maximum linear force of 585N was achieved to insert a large-diameter biopsy instrument in tissue during simultaneous MRI.

SMA/P actuators

A shape-memory alloy (SMA) /polymer (SMP) actuator consists of an alloy/polymer that can retain its preset shape when heated. SMA/P actuators are popular for their bio-inspired working principle that mimics human muscles. It has the advantage of high output power density and is usually designed for robotic joint motion. Kalmar et al. [66] proposed an SMA wire actuator for short stroke length. A detailed study of the relationship between the stroke and temperature was performed [40], allowing the robot to be controlled with simple Pulse Width Modulation (PWM) signal. The maximum accuracy of 5.5 degrees with a mean displacement error of 0.69 mm was reported. The SNR loss of 10% was observed in a 3 T MRI scanner environment. To overcome the slow response time of SMA/P actuators, compact air/water cooling systems are designed as an integrated part of the actuator. Experiments have shown that SMA/P actuators cooled with water can double the speed compared to their counterparts cooled with air.

Optical, cable, and other actuation methods

An optically powered, miniaturized ($2.5 \times 2.5 \times 3.0$ mm^3) actuator was proposed by Mutlu et al. [45]. It worked with the principle of Lorentz force. The magnetic field of the MRI scanner generated force/torque in a current-carrying coil. The photovoltaic cell embedded in the coil can generate a current from a wireless optical source. This initial wireless and modular actuator design can generate a unidirectional motion with a torque output of 100—200 μNm. An actuation power source outside the MRI room or gantry with traditional motors and transferring torque to the robot by a cable mechanism can also be used. They have the advantage of being flexible [61] and allowing long [67] range torque transmission. The latency and friction loss were key issues for this type of actuation. A long-range mechanism with low friction, high torque transfer, and small latency can be useful for MR conditional robots with complex motion capability.

Sensing

Thus far, extensive progress has been made in sensing for MRI-guided robot control and among which optical fiber-based methods are particularly useful [22, 68–70]. Optical-based sensors are used in application scenarios such as shape sensing and force/torque sensing. MR-based sensors represent an alternative approach and they are mainly used for target localization and direct temperature sensing. In Fig. 3, optical-based and MR-based sensors are summarized based on their sensing strategies. This subsection will focus on sensing principles based on these two sensing principles and their key characteristics and application areas are summarized in Table 2.

Optical based sensing

Light can propagate in different media such as air, water, fiber, and glass. Transmission of light in an optical fiber can be easily connected to a signal interrogator to derive a variety of optical information (wavelength, phase, frequency, and intensity. What's more, optical fibers are naturally MR safe because they are typically made of silica with a polymer coating. Furthermore, optical fibers can transmit signals for long distances with good stability. This is desired for transmitting signals between the MR scanner room and the control room. For this reason, many optical fiber-based sensors have been designed for MRI-guided surgical robot systems [82]. What's more, with the photoelectric effect, electrons can be ejected from the surface of the metal when light shines on a metal. Propagating light in the air enables vision-based sensing for the MRI-guided surgical robot [83]. Based on this, sensing strategies such as fiber Bragg grating

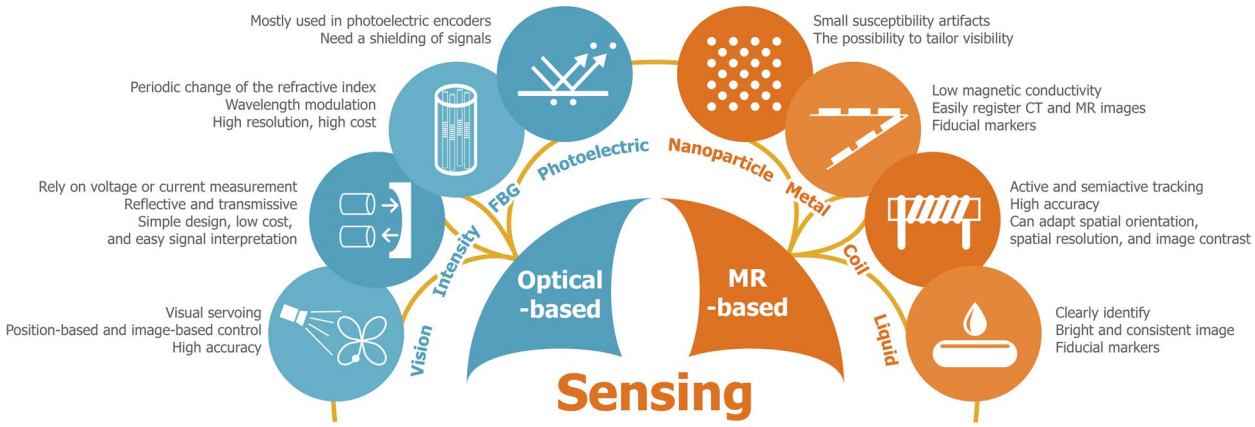

Fig. 3 Typical MR conditional/safe sensing methods. 1) Optical-based: FBG (for shape [71], force/torque [68], actuation [72] and temperature [69] sensing), intensity (for force/torque [73, 74] and actuation [75] sensing), photoelectric [42] (for actuation sensing), and vision [11] (for position sensing); 2) MR-based (for localization): active/semiactive coil [22, 76], passive metal [77], passive liquid [78], and passive nanoparticle [79]

(FBG), intensity, photoelectric, and vision can be used and they are illustrated in Fig. 3.

a) FBG based Sensors

The working principle of an FBG sensor is based on the radiation reflection of Bragg grating [82]. When an FBG fiber optic is interrogated with polychromatic radiation, a specific range of wavelengths is reflected by the FBG. The wavelength of the reflected wave will change as the strain of the gratings changes. Multiple sensing applications can be realized by using this principle, such as shape sensing, force sensing, torque sensing, actuation sensing, and temperature sensing.

1) *FBG-based shape sensing*: By using a multicore fiber with FBG distributed along the fiber, the shape of the fiber geometry can be precisely detected in a thin cross-sectional size. Jäckle et al. [71] used a piecewise constant curvature model to reconstruct the shape of the fiber. Its use for endovascular intervention showed an average and maximal error of 1.13 mm and 2.11 mm, respectively. This type of shape sensing fiber is MR safe, and it could be easily integrated into many MR conditional endovascular interventional instruments [22]. 2) *FBG-based force sensing*: A typical method for force sensing is to integrate multiple FBG fibers on the instrument. Fibers undergo strain when the device changes shape due to an external force. By using the static model between the external force and the strain of the FBG's position, the external force can be obtained. Elayaperumal et al. [80] integrated three fibers on the needle's inner stylet, 120° apart in the needle cross-section for tip force detection with a calibration error of 0.001 N. 3) *FBG-based torque sensing*: By arranging the FBG fibers on the instrument in different directions, it is possible to detect torque according to the static relationship. Monfaredi et al. [68] developed a structurally inherent decoupled sensor for force and torque measurement with temperature compensation. The force and torque sensing range of it were -20 to 20 N with 0.1 N resolution and -200 to 200 Nmm with 1 Nmm resolution. 4) *FBG-based actuation sensing*: Typical actuation sensing is via linear and rotary sensing. By using bespoke mechanical structures, the linear motion or rotation could be converted into the strain of FBG sensors. Huang et al. [72] developed an MR safe absolute rotary encoder based on eccentric sheave and FBG sensors with a high resolution of 0.1°. The eccentric sheave transformed the rotation of the shaft to the bending deflection of the beam, on which the FBG sensors are integrated. 5) *FBG-based temperature sensing*: Changes in temperature can result in small deformation of the optical fiber. Such small changes in strain can be obtained via wavelength changes of the reflected wave in the FBG fiber sensors. Saccomandi et al. [69] used 12 FBG sensors to monitor heating and cooling effect during LITT.

b) Intensity based sensors

The intensity of light can be measured and modulated for intensity sensing. There are many ways (reflective, two or more fibers light coupling, and macro bending) [70] to change the intensity of light passing through the fiber. And these principles could be used in force, torque, and actuation sensing of MRI-guided surgical robot systems.

1) *Intensity-based force sensing*: Some sensitive structures can vary the position and orientation of the integrated reflector when a force is applied to this structure. The intensity of the light would change because of the shift of the reflector. Polygerinos et al. [73] designed a force sensor consisting of three single optical fibers and a reflector that was allowed to move freely in all direc-

Table 2 Different sensing modalities for MR-safe/conditional robots

Type	Method	Application	Dimension (mm)	Range	Accuracy/Resolution	Comments	Refs
Optical-based	FBG	Shape	Φ 0.4 × 380	NA	2.11 mm / NA	High accuracy Long shape sensing	Jäckle (2019) [71]
		Force sensing	Φ 1 × 8	0.25 N	0.001 N / NA	High accuracy	Elayaperumal (2014) [80]
		Torque	Φ 15 × 20	± 20 N ± 200 Nmm	NA / 0.1 N NA / 1 Nmm	Torque and force sensing	Monfaredi (2013) [68]
		Actuation sensing	Φ 35 × 60	360°	1.61° / 0.1°	Absolute continuous sensing High resolution	Huang (2021) [72]
		Temperature sensing	NA	60 °C	NA	Large temperature range	Saccomandi (2014) [69]
	Intensity	Force	Φ 4 × 24.5	0.5 N	0.03 N / < 0.01 N	Low cost Three-axis sensing	Polygerinos (2013) [73]
		Torque	88 × 84 × 20	± 5 Nm	NA	MR safe Milling machining process	Gassert (2008) [74]
		Actuation sensing	Φ 58 × 80	360°	0.025°	High accuracy	Micronor Sensors [75]
	Photoelectric	Actuation sensing	Φ 35 × 5	360°	NA / 30°	Shielded and low SNR loss	Hofstetter (2022) [42]
	Vision	localization	≈Φ 2	NA	0.2 mm / NA	Fiber optic camera High accuracy	Fang (2021) [11]
MR-based	Passive-metal	localization	8 × 8 × 0.1	NA	NA	High marker-to-background contrast	Alipour (2018) [77]
	Passive-nanoparticle	localization	Φ 0.889	NA	NA	Artifact size can be changed	Nijsink (2022) [79]
	Passive-liquid	localization	Φ 15	NA	1.59 mm / NA	Integrated on robot	Stoianovici (2018) [78, 81]
	Active-coil	localization	Φ 2.67 × 115	NA	1.53 mm / NA	Coupled with FBG sensors	Dong (2022) [22]
	Semiactive-coil	localization	Φ 2.7	NA	NA	Image-Based Tracking	Eggers (2003) [76]

tions by mounting it on a sensitive structure (flexure). The sensing range was 0.5 N, and the accuracy was 0.03 N. 2) *Intensity-based torque sensing*: Similar to the principle of force sensing, the deformation of the sensitive structure has a defined static relationship with the external torque. Gassert et al. [74] developed a series of force/torque sensors with different materials and fabrication processes. Both the optical and mechanical parts of these sensors had a linear response to the measured directions but were immune to transverse forces and torques. The MR safe sensor was made of polyoxymethylene (POM) and can detect torque ranging from -5 Nm to + 5 Nm. 3) *Intensity-based actuation sensing*: Analogous to the conventional photoelectric encoders, a rotating disk that contains a unique pattern can be used to unambiguously reference the angular position of the disk. The optical power from the broadband light source is dispersed over the pattern of the disk and portions of the light spectrum are reflected through the system. Micronor *Inc*. used this method to develop MR safe encoders for MR environments [75].

c) Photoelectric sensors

When light shines on a metal, electrons can be ejected from the surface of the metal in a phenomenon known as the photoelectric effect. This method has been widely used in photoelectric encoders. Because this type of encoder would produce a current on the metal components when it is working, it is MR conditional and may affect the imaging quality of MRI. Therefore, the key point of this type of sensor is the shielding of signals both inside and outside the sensor, ensuring that the external RF signal does not affect the sensor's function and that the signal generated inside does not affect the MRI. Hofstetter et al. [42] developed an MR conditional electromagnetic servomotor with a photoelectric rotary encoder. The encoder and the motor rotor were housed in a continuous copper shield, and the power and control signal were transmitted by a double-shielded Cat7 ethernet cable with traps. The maximum SNR loss was only 1.5% in all tested scenarios.

d) Vision sensors

Visual servo control is a common control strategy in robotics. Since conventional cameras are not MR conditional, proper shielding measures and component replacement are required. A commercial MR conditional camera (MRC systems GmbH, Heidelberg, Germany) has been developed for motion tracking for marker-based optical tracking. Another commonly used vision camera is the MR conditional fiberscope which can be used in a narrow environment. Fang et al. [11] used a fiberscope to monitor the laser spot footprint and provide closed-loop guidance for laser beam steering control. Control of the laser spot on the mucosa along the prescribed trajectory was achieved through machine learning-based visual servo control. Accurate laser spot steering was achieved with a mean tracking error of < 3 pixels (~ 0.2 mm).

MR based sensing

Direct MR based sensing can be broadly classified into active/semiactive [22, 76] and passive [77, 78, 84] sensing modalities. In the magnetic field, protons absorbing energy at a specific frequency will reemit energy in the form of magnetic waveforms at the same frequency [85]. When clusters of local waveforms pass through the closed loop coil and change magnetic flux, the coil circuit resonates and then transmits amplified signals. This creates a high imaging contrast, thus allowing the active tracking of MRI-guided surgical robot systems. However, the magnetic field inhomogeneity greatly affects the imaging quality, which may cause some image artifacts. Artifacts can be used as markers for the positioning of the robot if the shape size of the artifact is determined and the artifact does not affect the overall image quality. Therefore, MR visible passive markers, such as metal, nanoparticles, and liquid capsules, could be used for localization in the image coordinate system. This subsection will highlight the current localization strategies based on direct MR based sensing, as shown in Fig. 3.

a) Passive sensing

A passive marker consists of an encapsulated volume of material that can be used to provide good contrast in the acquired imaging slices. The received MR signal is amplified by the passive markers to enhance the imaging contrast. The passive tracking method is efficient and flexible in identifying the location of the device. However, its main disadvantage is being scanner and material dependent. 1) *Metal*: Some non-magnetic metals with low magnetic conductivity could be used in MR environment. Au is widely used in prostate cancer as a marker [86]. Gold Anchor (Naslund Medical AB, Huddinge, Sweden) is a good fiducial marker intended to reduce the risk of marker migration. Alipour et al. [77] proposed passive coil markers consisting of two metal traces in the shape of a square with upper and lower traces connected to each other. The resonant coil enabled precise and rapid visibility at low background flip angles (6–18°). Such markers can also be used in MRI-guided surgical robots by combining them with interventional instruments or other components of the robot. 2) *Nanoparticle*: Thus far, magnetic nanoparticles have been used for diverse applications, including magnetic biosensing, magnetic imaging, magnetic separation, drug and gene delivery, and hyperthermia therapy etc. [84]. They can be easily detected by MRI. Hence combining magnetic nanoparticles with interventional instruments or MRI-guided surgical robot is an important direction to pursue. Nijsink et al. [79] integrated iron(II, III) oxide (Fe_3O_4) nanoparticles on a guidewire for identification. The results showed that marker visibility was sufficient and a large range of artifact sizes can be generated. 3) *Liquid* capsule:

The liquid capsule could clearly identify areas of interest in MRI with a bright and consistent image. Because the position of those liquid capsules in the robot's coordinate system is known, so the robot's coordinate system to the MRI coordinate system needs to be registered by detecting the markers on an MR image. There are many commercialized liquid capsules that can be used for localization in MRI. [81]. Stoianovici et al. [78] used MRI imaging liquid capsules (Beekley Corp., Bristol, CT) for the registration of the robot. Because simple thresholding did not always provide robust automatic detection due to noise from other sources, four cylindrical MR-visible markers were arranged into the link of the RCM module. The experiment showed that the MRI-guided targeting accuracy and precision in vitro were 1.71 mm and 0.51 mm.

b) Active/semiactive sensing

Active tracking refers to the principle of an active element attached to the device transmitting a signal from within the body and the imaging modality that receives these signals. Active tracking sensors are typically composed of several loops of current-carrying wire, capacitors, and peripheral electronic components [87]. 1) *Active*: An active marker is a micro-coil receiver that provides an MR signal to a dedicated channel of the MRI system. The MR system could activate the small coils by RF pulse and then selectively pick up resonating signals around these coils. Dong et al. [22] developed a shape tracking system that integrated a multicore FBG fiber and active tracking coils with a standard cardiac catheter. The feedback control performance was tested by autonomous targeting and path following based on these two sensing strategies. 2) *Semiactive*: A semiactive marker serves as a resonant microcircuit, inductively coupled to a receiver coil of the MRI system. Eggers et al. [76] proposed a robust localization method of parallel resonant coils. This method circumvents most of the drawbacks usually associated with image-based tracking, such as low temporal resolution.

Materials

Material requirements

Challenges in developing MRI-guided robots mainly arise from the MR characteristics of materials used for robot components (*e.g.*, actuators, positioning sensors, bearings, and other hardware) and intervention devices (*e.g.*, guide wires, needles) that would cause MRI artifacts, heat generation, loss of positioning accuracy in MR environment [34]. Figure 4 illustrates the microstructures of four potential MR safe/conditional materials, including metal, bulk metallic glass, polymer, and ceramic. Table 3, summarizes their physical, mechanical, and electromagnetic properties given in the literature.

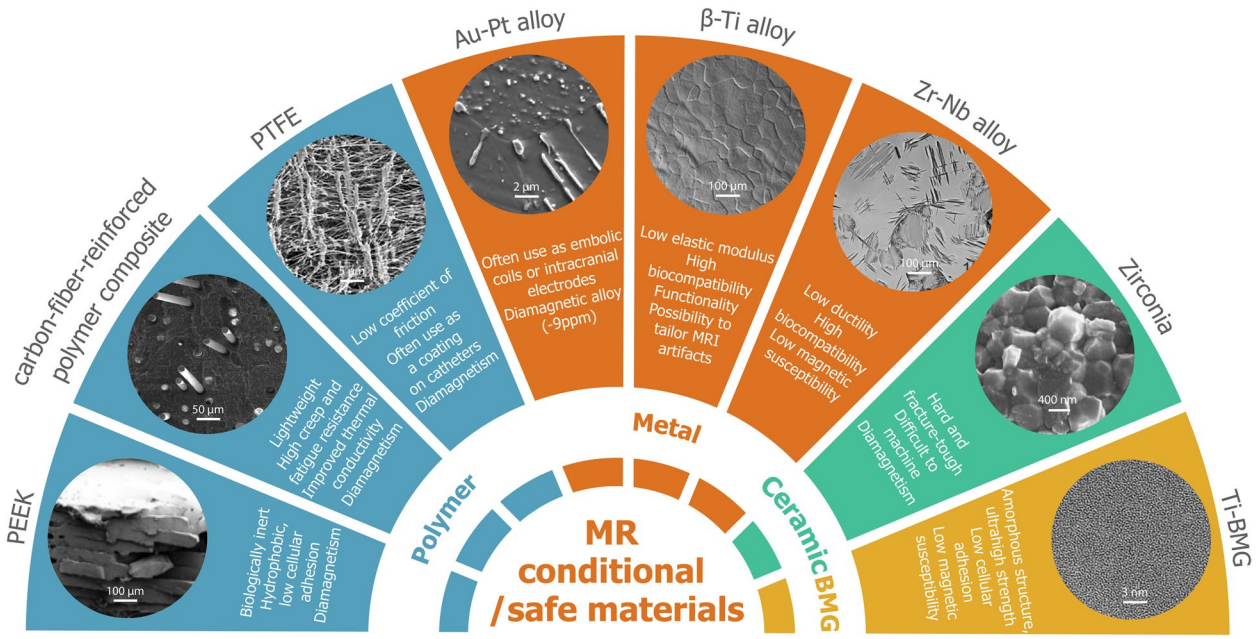

Fig. 4 Commonly used MR conditional/safe materials. Metals such as Au-Pt [97], β-Ti [98] and Zr–Nb [99] alloys can combine mechanical property and MRI compatibility by microstructure design and control; Bulk metallic glasses (BMGs) such as Ti-BMG in amorphous structure exhibits relatively low magnetic susceptibility [32, 100]; Polymers such as PTFE [101] and PEEK [102] do not generate MRI artifacts due to their inherent diamagnetism, and polymer matrix composites (*i.e.*, carbon-fiber-reinforced polymer composite) exhibit synergetic effect combining MRI compatibility of polymer with the stiffness and strength of carbon fibers [103]; Ceramics such as zirconia generate negligible susceptibility artifacts and can use as needle tip [104, 105]

Requirements of MR conditional/safe materials

MRI artifacts are generally attributable to susceptibility-related artifacts and electromagnetic induction-related artifacts [36]. Since metals are conductive, electromagnetic induction-related artifacts of metallic devices are unavoidable but can be reduced by optimization of the metal's electrical conductivity or the shape of metallic implants. The selection of materials with low susceptibility is a practical solution for improving the MR safety of devices. A concept for the design of materials with low magnetic susceptibility has been developed [36]. This can be achieved via: (i) alloying paramagnetic metal with diamagnetic metal; (ii) precipitation of a diamagnetic or low magnetic susceptibility phase in a paramagnetic matrix phase; and (iii) formation of composite of paramagnetic metal and diamagnetic material.

Considerations should also be taken to avoid RF-induced heating in electrically conductive instruments in strong electromagnetic fields. RF-induced heating not only depends on the geometric configuration and arrangement relative to the RF transmit coils and the parameter settings of the MR sequence but also on the device properties, such as electrical conductivity and permittivity [106]. Preferably, diamagnetic materials such as ceramics and polymers should be used to avoid inductive heating.

Apart from electromagnetic characteristics, suitable materials should also exhibit advantages in aspects of mechanical properties, corrosion resistance, processability, as well as biocompatibility for the components that come in direct contact with patient's tissue. For instance, in designing an ideal MR conditional microwave needle for MRI-guided interventional microwave ablation, the consideration for material selection is on the comprehensive performance of mechanical properties (including rigidity, toughness, and puncture force), needle artifact configuration, needle visibility, and ablation performance under a strong magnetic field [104].

Dependence of microstructure on magnetic susceptibility

Magnetic susceptibility is a quantitative measure of a material's tendency to interact with and distort an applied magnetic field. The magnetic susceptibility of crystalline alloys is largely dependent on the chemical concentration and phase constitution, as well as the dependency roughly follows Wiedemann's additivity law [107]. For instance, in Zr–Nb alloy, the phase composition evolves with decreasing Nb content as follows: $\beta \rightarrow \beta+\omega \rightarrow \beta+\omega+\alpha' \rightarrow \alpha'$ phase. And their magnetic susceptibility ($\chi_{Zr\text{-}Nb}$) is expressed as [108]:

$$\chi_{Zr-Nb} = V_{\beta} \cdot \chi_{\beta} + V_{\alpha'} \cdot \chi_{\alpha'} + V_{\omega} \cdot \chi_{\omega}$$

where χ_{β}, $\chi_{\alpha'}$, χ_{ω} and V_{β}, $V_{\alpha'}$, V_{ω} are the magnetic susceptibility and volume fraction of β, α′, and ω phases, respectively. The magnetic susceptibility χ_v of each phase is in the sequence: $\chi_{\beta} > \chi_{\alpha'} > \chi_{\omega}$, suggesting that the material composed of single ω phase exhibits the lowest χ_v [108, 109]. As reported by Nomura et al. [99], as-cast binary Zr-(3–9)Nb (wt.%) alloy containing large amounts of ω phase showed a minimum magnetic susceptibility. Tuning Nb content yields the formation of β and α′ phases, which gives rise to an increase of χ_v. A similar tendency also exists in binary Zr-Mo alloy [109, 110] and Cu-Sn ($1.5 \leq Sn \leq 7.0$ at.%) alloy [111]. Noble Ag-Pd and Au-Pt alloys exhibit nonlinear dependence of χ_v on alloy composition throughout the entire composition range [32].

It is worth noting that the optimal microstructure should balance its effect on magnetic susceptibility and on mechanical properties as well. The ω phase, on the one hand, decreases the χ_v. On the other hand, the increased content of ω phase formed thermally in a needle-like shape, makes the material prone to brittle fracture. After appropriate annealing treatment, Zr-(14–20)Nb(wt.%) alloys consisting of mainly β phase with a small amount of lenticular ω phase exhibit low magnetic susceptibility, low Young's modulus and enhanced elongation [108]. Therefore, magnetic compatibility can be tailored by microstructure control. The effect of microstructure on mechanical reliability should also be taken into consideration according to the application requirements of medical devices under MRI.

Material selection

Stainless steel

In MR environment, stainless steels heavily distort MRI images and lead to significant MRI artifacts due to their ferromagnetic and electromagnetic characteristics. The interventional probes and instruments made of stainless steel may cause the loss of positioning accuracy or RF-heating during surgical operations and, therefore, are undesirable for MRI-guided interventional procedures. Patients with stainless-steel implants such as dental braces and coronary stents [88] should be avoided exposure to an MR environment. It is necessary to develop suitable MR conditional materials satisfying all requirements of no toxicity, high corrosion resistance, and high electric conductivity for biomedical applications.

Ti-based alloys

Ti and Ti-based alloys have been widely used for medical applications due to their excellent combination of low density, good corrosion resistance, high mechanical performance, and good biocompatibility. Joint replacements, surgical screws, bone plates, pacemakers and puncture needles made from Ti-based alloys and NiTi shape memory alloys are commercially available [112]. In terms of its use under

Table 3 Physical, mechanical and electromagnetic properties given in literatures for the investigated materials in this review

Type	Material	Magnetic susceptibility,χ_v, (ppm)	Electrical Conductivity (S/m)	Young's modulus (GPa)	Yield/Ultimate strength (MPa)	Density (g/cm^3)	Comments	Refs
Metal	Stainless steel	3520 ~ 6700	1.45×10^6	193	/580	8	Generate severe susceptibility artifacts Good machining property	Holton (2002) [88]
	Cu	-9.63	5.8×10^7	119	/200	8.96	High thermal and electrical conductivity Its magnetic susceptibility close to water and tissues	Ihira (2016) [89]
	Brass	-0.22	5.88×10^7	105	/340	8.47	Malleability and machinability Antibacterial property	Schenck (1996) [33]
	Ti	182	2.38×10^6	116	/220	4.5	High strength-to-weight ratio High corrosion resistance	Tse (2011) [31]
	Ti-6Al-4 V	179	5.6×10^5	110	/950	4.43	Excellent strength-to-weight ratio Not easy to machine due to low heat conductivity and high flexibility	Fonda (2008) [90]
	β Ti-Zr based	50	NA	45	/900	5.89	Low elastic modulus High biocompatibility Functionality (superelasticity, shape memory effect)	Calin (2021) [91]
	Zr	109	2.37×10^6	110	/388	6.52	Low ductility Good machining property	Schenck (1996) [33]
	Nb	237	7.00×10^6	103	/275	8.57	Good machining property	Schenck (1996) [33]

Table 3 (continued)

Type	Material	Magnetic susceptibility,χ_v, (ppm)	Electrical Conductivity (S/m)	Young's modulus (GPa)	Yield/Ultimate strength (MPa)	Density (g/cm^3)	Comments	Refs
	Al	20.7	3.77×10^7	70	/90	2.7	Low density Good machining property	Schenck (1996) [33]
	Au	-34	4.11×10^7	79	/120	19.3	High malleability and corrosion resistance Diamagnetism	Schenck (1996) [33]
	Ag	-24	6.30×10^7	83	/140	10.49	Highest electrical and thermal conductivity Diamagnetism	Schenck (1996) [33]
Bulk metallic glass	Au-based	-38	NA	74.4	1049/	11.6	Diamagnetism Good machining property	Zhou(2016) [32] Schroers (2005) [92]
	Cu-based	133	NA	102.1	2050/	7.0	High strength Poor corrosion resistance High glass-forming ability	Zhou (2016) [32]
	Zr-based	95	NA	82.8	1600/	6.5	Good tribological and wear-resistant properties Superior glass-forming ability	Zhou (2016) [32]
	Ti-based	163	NA	100.4	2010/	6.3	Usually contain toxic elements Low glass-forming ability Lightweight high-strength	Zhou (2016) [32] Pang (2015) [93]

Table 3 (continued)

Type	Material	Magnetic susceptibility,χ_v, (ppm)	Electrical Conductivity (S/m)	Young's modulus (GPa)	Yield/Ultimate strength (MPa)	Density (g/cm^3)	Comments	Refs
Polymer	PEEK	NA	$10^{-13} \sim 10^{-12}$	3.5	/100	1.26	Hydrophobic surface limiting cellular adhesion	Tse (2011) [31]
	POM	-9.36	10^{-15}	3.16	/70	1.43	High creep (as compared to nylon) and fatigue resistance	Wapler (2014) [94]
	PTFE	-10.28	$10^{-25} \sim 10^{-23}$	0.625	/28	2.12	Often use as a graft material in surgery and as a coating on catheters Not easy to machine due to low coefficient of friction	Tse (2011) [31]
	Nylon	NA	NA	4	/40	1.25	Good creep resistance Good machining property	Tse (2011) [31]
	Carbon fiber	NA	10^{-13}	96	/1250	1.6	Lightweight, high stiffness and tensile strength High thermal and electrical conductivity	Tse (2011) [31] Mirdehghan (2011) [95]
Ceramic	Alumina	-18.1	1.5×10^{-7}	370	/300	3.96	Difficult to machine due to their extreme hardness, non-electrical conductivity and brittleness	Tse (2011) [31]
	Zirconia	-8.3	$2 \times 10^{-6} \sim 6 \times 10^{-5}$	100–250	/330	5.68	Must be machined carefully as the zirconium powder and shavings are flammable	Schenck (1996) [33] Kwon (2017) [96]

MRI, pure Ti and Ti-6Al-4 V alloy, with volume magnetic susceptibilities of 182 ppm and 179 ppm, respectively, cause large MRI artifacts. β-Ti alloys, alloying Ti with low susceptibility elements such as Zr, Mo and Sn, are expected to display reduced artifacts. β-metastable Ti-Zr based alloys have been designed to exhibit very low magnetic susceptibility where ω phase was formed. In addition, β- metastable Ti-Zr-based alloys can exhibit functional properties [113, 114], such as shape memory effect and superelasticity. These alloys can be used for guide wires, orthodontic arch wires, endodontic reamers, and files. Furthermore, Mariana et al. [91] designed novel MR conditional glassy Ti-Zr–Nb-Hf-Si alloys with weak paramagnetic nature (ultralow magnetic susceptibility of ~ 50 ppm) and superior radiopacity (high X-ray attenuation coefficients). For satisfying performance in both mechanical properties and MR safety, the BMG materials are of interest especially for making interventional devices with minimized MRI artifacts [32, 115].

Zr-based alloys

Zr and Ti are elements in VI B group, which have similar physical and chemical properties. Compared with Ti, Zr has a lower magnetic susceptibility and cytotoxicity, and a high corrosion resistance due to passive oxide formation on its surface. Unalloyed Zr is not mechanically reliable to serve as structural materials. Alloying is effective in improving the mechanical strength and can further decrease the magnetic susceptibility of alloys. Zhou et al. [116] surveyed systematically in Zr-1X alloys (X = Ti, Nb, Mo, Cu, Au, Pd, Ag, Ru, Hf, and Bi) and found good performance in strength, ductility, in vitro cytocompatibility, and magnetic susceptibility for Zr-1Ru alloy. It is a potential candidate material for MR conditional medical devices. Zr-3Mo and Zr-9Nb alloys show low magnetic susceptibilities but poor formability and machinability. This is because the presence of ω phase is contributable to the minimization of magnetic susceptibility but limited to their tensile strength and ductility.

Au-based alloy

Au is a diamagnetic metallic element with high biocompatibility, high mechanical performance and high corrosion resistance. Kodama et al. [117] reported that, by alloying diamagnetic Au with paramagnetic Pt, Au-35Pt alloy showed a volume magnetic susceptibility of -8.8 ppm. This value is very close to that of body tissue (-11 ~ -7 ppm), which makes the alloy almost free from MR imaging artifacts. However, the single-phase Au-35Pt alloy exhibits poor machinability with low ductility. Ryusuke et al. [97] developed dual-phase Au-30Pt and Au-33Pt alloys. They not only are free from magnetic susceptibility artifacts, but also have improved workability for producing various implantable medical devices. For example, it can be used to make embolic coils treating intracranial aneurysms or intracranial electrodes. Most importantly, there is no difficulties in performing examinations using MRI for patients with implants made of dual-phase Au-Pt alloys.

Polymers and ceramics

To reduce susceptibility-related artifacts, attempts have been made to replace metallic materials with polymers and ceramics. Polymers (such as polytetrafluoroethylene (PTFE), polyetheretherketone (PEEK), polyoxymethylene (POM), and acrylonitrile butadiene styrene (ABS)), polymer matrix composites (such as glass fiber or carbon fiber reinforced polymers) and ceramics (such as alumina, zirconia) generally exhibit low susceptibility and present small artifacts. MR conditional puncture needles and guide wires in glass-fiber-reinforced plastics are commercially available. Hempel et al. [118] constructed the main frame of the MRI-guided surgical robot using fiber-reinforced epoxy and PEEK. To develop an MRI-guided robot for prostate interventions, Stoianovici et al. [119, 120] used nonmagnetic and dielectric materials such as plastics, ceramics, and elastomers to ensure the system is MR safe. Nevertheless, for the polymers used within or close to the imaging zone of the MR system, MR artifact testing should be performed. On the one hand, polymers contain hydrogen protons which can generate MR signals to disturb the image and degrade the image quality. On the other hand, polymers can also contain dotting with ferromagnetic debris from manufacturing, causing significant artifacts.

Although polymers and ceramics are likely to more friendly to MR conditional devices, there is still a need for metallic materials. This is because metals are conductive, have unique mechanical property, and is visible in radiographs. The optimal structural design of components is to combine the advantages of metals, polymers, and ceramics. Huang et al. [104] proposed an MR conditional needle consisting of a zirconia tip and TA18 (Ti-3Al-2.5 V, at.%) titanium alloy tube coated with Teflon, which provides good mechanical properties, reliable MRI visibility for positioning and monitoring, and insignificant RF-induced heating.

Mechanical properties and fabrication considerations

Formability and machinability

Formability and machinability depend on both material properties (*i.e.*, chemical composition, microstructure, hardness, tensile strength and thermal conductivity) and machining process parameters (*i.e.*, the rigidity of tool, and cutting parameters such as feed, speed and cutting force). Generally

speaking, hardness decreases machinability due to the high-power consumption and tool wear. Ceramics are hard to machine due to their brittleness and high hardness. Metals and some polymers with high strength, such as PEEK, are usually for conventional machining. Other polymers, such as Delrin and ABS, can be precisely cut by a water jet cutter. The polymer matrix composites reinforced by glass fiber or carbon fiber have intermediate mechanical properties between metals and polymers but have poor machining properties due to fibers.

Anisotropy of magnetic and mechanical properties for alloys and components

The crystallographic texture is commonly developed in materials and significantly affects the physical, mechanical, and electromagnetic properties of materials. Zhang et al. [121] found a clear crystallographic anisotropy of the superelasticity and mechanical responses in β-Ti2448 single crystals oriented in $<100>_{\beta}$, $<110>_{\beta}$, and $<111>_{\beta}$. Due to macroscopically well-organized materials with anisotropic electron configurations, an orientation-dependent magnetization or magnetic susceptibility anisotropy is the intrinsic nature characteristic [122]. For materials with anisotropic microstructure, the orientation of the fibers can affect the imaging performance. Therefore, knowledge of orientation-dependent behavior is highly desirable in order to optimize the performances of tools and devices.

Fonda component design based on additive manufacturing

Additive Manufacturing (AM) is attracting extensive attention for robot construction. Different from conventional manufacturing processes such as casting, forging, and powder metallurgy, AM fabricates components by melting and reconsolidating raw materials layer by layer as designed, with no need for tooling and machining. This prevents the wastage of workpiece materials and saves the consumption of machining resources. Another advantage over conventional manufacturing routes is the neatly unlimited design flexibility, which provides opportunities to select and combine the properties of different materials to fabricate complex components with high performances. However, due to excessively fast consolidation, it is tricky to optimize AM parameters to control the microstructural uniformity and the distribution of residual stress, which are essential to quantifying the performance of devices obtained from AM. Overall, AM will be an efficient technique for fabricating medical devices with complex geometries and specific function requirements, such as soft actuators and robots that can be used in MRI-guided interventions [123].

Interventional instruments

Intervention is a commonly practiced procedure for both diagnosis and treatment. Many MRI-guided robots can carry out a variety of intervention procedures such as ablation, neuromodulation, biopsy, catheterization, etc. For interventional instruments, MR safety is crucial. In addition, the interventional instruments should be easy to be integrated into the MRI-guided robotic system. Since accurate intervention requires either image or marker guidance, MR conditional guidewires and markers are also included in this review. In addition, commercially available interventional devices and guidance components and non-commercial devices that are developed in research labs are also discussed. Figure 5 summarizes typical interventional instruments that can be used for MRI-guided robots according to five categories: ablation, neuromodulation, biopsy, catheterization, and others. This section also includes corresponding application scenarios and potential applications of MRI-guided robots as shown in Table 4.

Ablation

LITT is a minimally invasive treatment modality that uses the laser for thermal ablation [149]. It has been used in treating diseases such as tumors [150] and necrosis. With the development of MRI, LITT has been used in various MRI-guided therapies, especially for treating unresectable glioblastoma [151]. For MRI-guided LITT, laser probes are used for intervention. Precise positioning of the laser probe is crucial for treatment. Early work using the NEUROGATE® system used an interventional 0.5 Tesla MRI (Signa SP, GE, USA) for LITT guide (Dornier GmbH, Germering, Germany) with the sheath (Somatex GmbH, Rietzneuendorf, Germany) [133]. Till now, two MR conditional LITT systems are FDA-approved: Neuroblate ® (Monteris Medical, *Inc*., Plymouth, MN, USA) [17] and Visualase ® (BioTex, *Inc*.; Houston, TX, USA) [134].

Different to LITT, MRgFUS uses focused ultrasound for thermal ablation [152]. ExAblate system (InSightec, Haifa, Israel) is FDA-approved for both 1.5 T and 3 T MR scanners [135]. It has been used to treat brain, body, and prostate. For example, the ExAblate Neuro 4000 system has a hemispheric transducer that is closely applied to the patient's skull via a stereotactic frame. The transducer has 1024 phased array ultrasound elements that can be individually controlled to allow for energy and phase selection [135]. Similar to LITT, another focused ultrasound application is interstitial MRI-guided focused ultrasound (iMRgFUS). It uses sonic waves to create an area of thermal energy that can destroy the target tissue. iMRgFUS is inserted through a cannula similar to LITT [126] and commercial transducers such as ACOUSTx applicators (Acoustic Medsystems, Savoy, Illinoi).

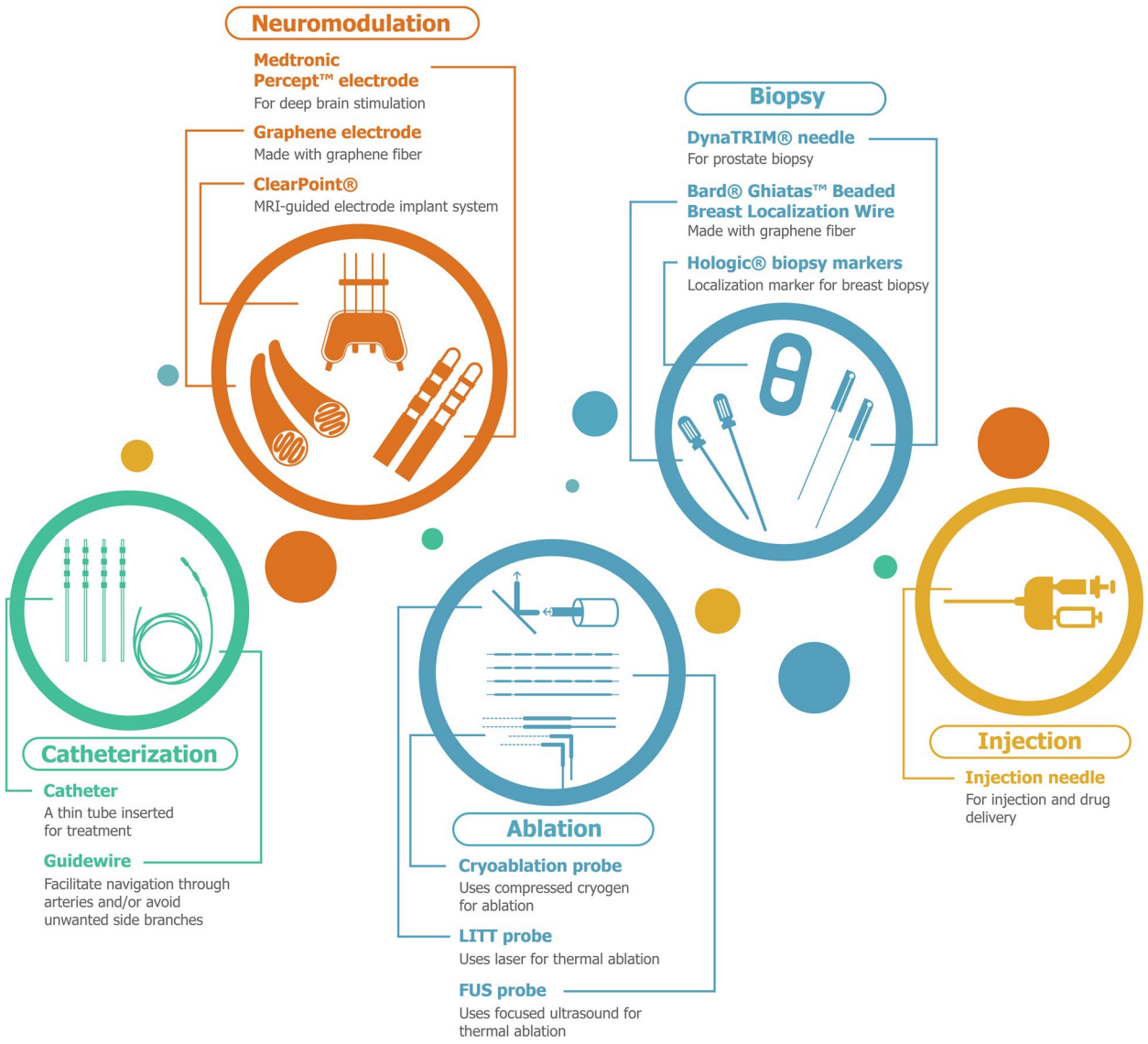

Fig. 5 Typical interventional instruments can be used for MRI-guided robots. Ablation: cryoablation probe [124, 125]; LITT probe [17]; FUS probe [126]. Neuromodulation: conventional electrodes; instruments for electrode implant [127]; electrode made of graphene [128]. Biopsy: biopsy needles [129]; biopsy markers; localization wire. Catheterization: catheter [130]; guidewire [131]. Others: injection needle [132]

Cryoablation uses a thin, wand-like needle called a cryoprobe to be placed directly into the target tissue. A compressed cryogen (argon gas or liquid nitrogen) is pumped into the cryoprobe to damage or destroy the tissue to create ablation lesions. Then the tissue is allowed to thaw. The freezing and thawing process is repeated several times. MRI-guided Cryoablation has been used for neurological [124], prostate [125], and cardiac [137] diseases. Commercial cryoablation systems include VISUAL ICE™ MRI from Boston Scientific [124, 125] and Medtronic CryoCath [137].

Radio Frequency (RF) ablation is operated at a frequency of approximately 500 kHz, interfering with MR imaging. However, microwaves between 915 MHz and 2.45 GHz do not affect MR imaging and are expected to provide an equivalent or greater efficacy than RF ablation [139]. In contrast to RF ablation, microwave ablation is independent of increasing tissue impedance that enables higher temperature and larger ablation zones in a shorter time with a single probe [138]. Based on a 0.5 T scanner (Signa, GE Healthcare, USA) and a microwave ablation system, real-time MR image guidance was used for liver tumor ablation [139]. Other MRI-guided microwave ablations include liver tumor treatment in a 1.5 T scanner and the development of novel ablation devices [104, 138].

Table 4 MR-safe/conditional interventional instruments

Intervention Procedure	Intervention	Organ/animal	System/device	Compatible Magnetic field (T)	Comments	Refs
Ablation	LITT	Brain	NEUROGATE®	0.5	Light guide with the sheath for LITT	Vitzthum (2004) [133]
	LITT	Brain	Neuroblate®	1.5	Laser probe diameter is 3.3 mm	Sloan (2013) [17]
	LITT	Brain	Visualase®	1.5	Laser probe diameter is 3 mm	Carpentier (2012) [134]
	MRgFUS	Brain, prostate, body	Exablate	1.5, 3	1024 phased array ultrasound elements	Jameel (2021) [135]
	iMRgFUS	Brain, liver	ACOUSTx applicators	3	Multielement high-frequency tubular piezoelectric transducers with a 360° insonation pattern mounted on a 13-G implant catheter	MacDonell (2018) [136]
	Cryoablation	Spine	Cryoprobes IceSeed™ MRI	1.5, 3	VISUAL ICE™ MRI system (Gauge 17G)	Moses (2020) [124]
	Cryoablation	Heart	Freezor™ MAX Cardiac Cryoablation Catheter	3	An MR conditional 28 mm cryoballoon developed from a clinical 28 mm arctic front advance cryoballoon	Kholmovski (2016) [137]
	Microwave ablation	Rabbit	MR conditional microwave needle	1.5	Zirconia tip and TA18 titanium alloy tube	Huang (2022) [104]
	Microwave ablation	Liver	ECO-100AI13C (Nanjing ECO Medical Instrument Co.)	1.5	14-G microwave applicator	Winkelmann (2020) [138]
	Microwave ablation	Liver	Microtaze (Model HSD20M, Alfresa Co.)	0.5	A 5 mm diameter bore scope with MR conditional needle	Murakami (2015) [139]
Neuromodulation	DBS	Brain	Medtronic Percept™ PC	1.5, 3	MR conditional probe	Medtronic [140]
	DBS	Brain	ClearPoint®	1.5	Intervention system for placing probes	Larson (2018) [141]
	DBS	Mouse	DBS-fMRI preclinical imaging	9.4	Probes made of graphene fibers	Zhao (2020) [128]
	Catheter	Brain shunt	Ares™ antibiotic-impregnated catheters	MR-safe	The shunt catheter is MR safe	Richards (2009) [142]
	Cranial stabilization	Head and neck	DORO LUCENT® iMRI Cranial Stabilization System MAQUET	1.5, 3	A standard rigid 3-pin fixation for head and neck surgery	Lang (2023) [143]
Biopsy	Biopsy	Prostate	DynaTRIM®	1.5, 3	The needle guide accommodates 18-G, 150 mm and 175 mm needles	Woodrum (2016) [129]
	Biopsy	Prostate	MRI Devices (Daum)	1.5	The needle guide is filled with contrast material gel that can be visualized at MR imaging	Beyersdorff (2005) [144]
	Biopsy and localization	Breast	Bard® Ghiatas™ Beaded Breast Localization Wire	1.5, 3	20-G, 9 cm, and 20 cm needles	Bard [145]

Table 4 (continued)

Intervention Procedure	Intervention	Organ/animal	System/device	Compatible Magnetic field (T)	Comments	Refs
Catheterization	Catheter	Brain	MR conditional Catheter	3	A 6.6 Fr guide catheter	Kilbride (2021) [130]
	Catheter	Heart	Terumo	3	A 5 Fr guide catheter using 0.1 mm diameter enameled copper wire	Heidt (2019) [146]
	Guidewire	Heart	EmeryGlide™	1.5	The angled tip is 0.035" (0.89 mm) in diameter and the wire is 180 cm	Veeram (2020) [131]
	Guidewire	Heart	EPflex	1.5, 3	The angled tip is 0.035" (0.89 mm) in diameter	Knight (2019) [147]
	Injection	Swine	The MR-Tracked injection needle	1.5	Two concentric titanium tubes (0.81 mm OD, 0.1 mm wall and 1.6 mm OD, 0.2 mm wall, respectively)	Schmidt (2021) [132]
	Injection	lumbosacral spine	SOMATEX® needle	1.0	20-G Chiba-type needle with a length of 100 or 150 mm	Streitparth (2013) [148]

Neuromodulation

Neuromodulation includes stimulation of the spinal cord, peripheral nerve, deep brain, vagal nerve, and sacral nerve. Readers are referred to a comprehensive review and guidelines of MR conditional devices for neuromodulation [153]. Here we briefly discussed the MR conditional devices for brain surgery and DBS. Typical neurosurgery procedures usually involve the fixation of the head for accurate imaging and positioning. Traditionally, a stereotactic frame is used but not MR conditional. The DORO LUCENT® iMRI Cranial Stabilization System MAQUET is MR conditional and suitable for intraoperative Magnetic Resonance Imaging (iMRI) [143]. This is especially important for positioning the head inside the head coil. A shunt is to place a tube in the brain to drain cerebrospinal fluid and redirects it to another location in the body where it can be reabsorbed. Shunt procedures can relieve intracranial pressure caused by hydrocephalus. Commercial MR conditional shunt devices include Medtronic StrataMR™ II valves and Ares™ antibiotic-impregnated catheters.

DBS is a treatment of neurological and psychiatric disorders by implanting electrodes into certain brain regions [154]. The electrodes generate electrical impulses for the modulation of neural networks and the precise placement of the electrodes is crucial for optimal treatment performance. MRI-guided DBS has become at the forefront of DBS practice and research [141]. The ClearPoint system is the first MRI-guided DBS [155]. It can achieve a projected radial error of < 0.5 mm, which is defined as the scalar distance between the intended target and the actual DBS lead location [156]. The intervention process includes using a ceramic stylet to reach the target during intervention scans [141]. Then, the MR conditional electrode is placed at the target. The same device sets were also used for catheter placement and drug delivery [127]. For MR conditional electrode probes, commercially available products include Medtronic Percept™ PC and Medtronic 3389 [157] for both 1.5 and 3 T scanners. New probes were also developed for different application scenarios. For example, graphene fiber showed to have superior MR compatibility in a 9.4 T preclinical scanner [128].

Biopsy

Biopsy is one of the most common interventional methods in clinical practice. MRI-guided biopsy has been used in breast [158] and prostate [159]. Besides biopsy, the intervention process to obtain a small piece of tissue sample is similar to that of placing radiative seeds or markers in the brachytherapy. Wire localization has been the standard procedure for breast biopsy for preoperative localization before the surgical removal of cancerous tissue. With this method, a wire is placed in the breast percutaneously, with the distal wire segment positioned adjacent to the abnormality. The MR conditional wire facilitates MR image guidance of the wire positioning, and there are many commercial products such as Ghiatas™ Beaded Breast Localization Wire. A variety of MR conditional markers are also available for surgical guidance such as Mammotome® and Hologic® markers. For in-gantry MRI-guided biopsy of prostate, the FDA-approved system is DynaTRIM (Invivo, Gainesville, Fl, USA) [160].

Catheterization

Endovascular intervention, or catheterization, is the primary method to treat cardiovascular disease. The intervention is to manipulate guidewires and catheters within the vasculature to reach certain blood vessels [28]. Before placing catheters, guidewires are used to navigate through the vasculature to reach the targeted vessel. Typical MR conditional guidewires include EmeryGlide™ (Nano4imaging, Düsseldorf, Germany) [131] and EPflex (Dettingen an der Erms, Germany) [147, 161]. A typical commercial MR conditional catheter is Terumo (Terumo Europe E.V., Leuven, Belgium) [162]. Besides endovascular intervention, MR conditional catheter was also developed for stroke treatment [130]. In addition, many MR conditional devices were also developed. Typical examples include injection [132]. One typical example is using MR image for guiding lumbosacral periarticular injection using an open 1.0 T MRI system with vertical field orientation (Panorama HFO; Philips, Best, the Netherlands). The MR conditional needle used is a 20-G Chiba-type needle (SOMATEX, Teltow, Germany and Cook, Bloomington, IN).

Interactive/real-time MRI

Interactive or real-time image guidance is a critical component for MRI-guided robots. Under the paradigm of MRI guided intervention, surgical planning, robot control, and feedback evaluation are all closely related to MR imaging. The increasing demand for high spatiotemporal resolution imaging, especially interactive/real-time imaging, is becoming crucial for improving the performance of MRI-guided robots. Here we first discuss key considerations for MR imaging including efficient k-space coverage, parallel imaging, and reconstruction techniques, followed by intraoperative guidance and visualization requirements. Figure 6 summarizes the application of these techniques in different clinical specialties. Table 5 detailes the characteristic of different intraoperative MRI sequences in robot-assisted surgery.

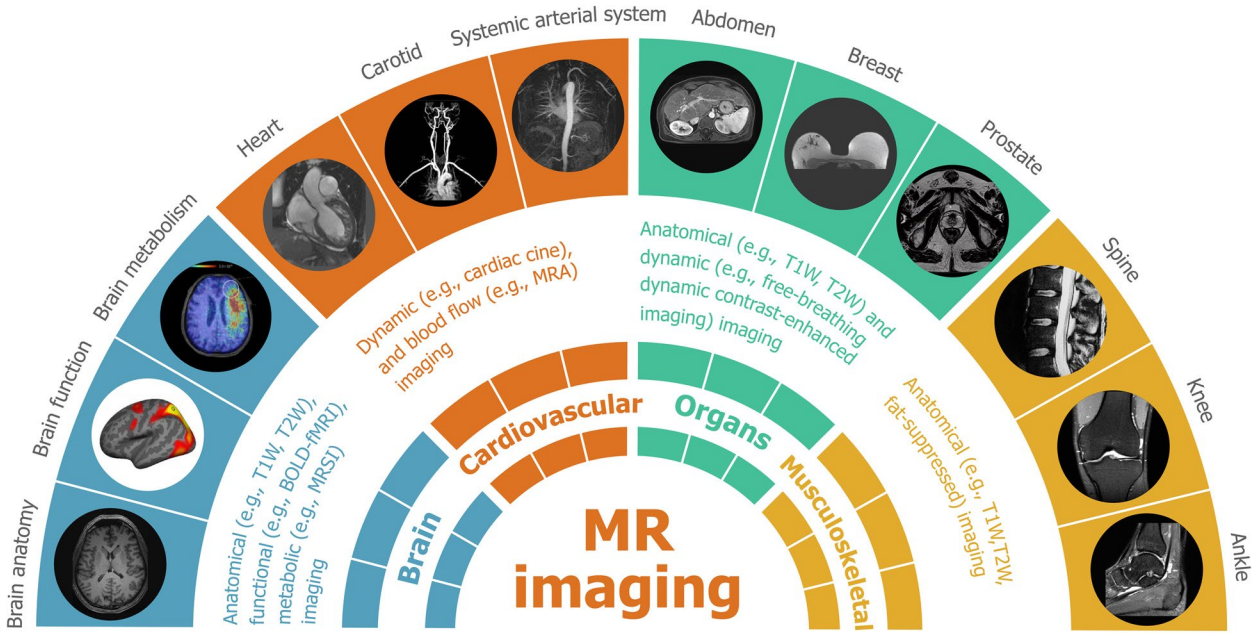

Fig. 6 Typical MRI sequences for pre- and intra-operative image guidance. MRI can provide anatomical (*e.g.*, T1W, T2W, fat-suppressed, and MRA), functional (*e.g.*, BOLD-fMRI), metabolic (*e.g.*, MRSI), and dynamic (*e.g.*, cardiac cine and dynamic contrast-enhanced imaging) information. Typical clinical applications include brain (*e.g.*, anatomy, function, and metabolism), cardiovascular (*e.g.*, heart, carotid, and systemic arterial system), various organs (*e.g.*, abdomen, breast, and prostate), and musculoskeletal (*e.g.*, spine, knee, and ankle) imaging [163–166]

Considerations for MR imaging

As mentioned earlier, MRI is intrinsically a multimodal imaging method that can provide anatomical, functional, and metabolic information. Typical anatomical imaging methods include T1-Weighted (T1W), T2-Weighted (T2W), MR Angiography (MRA), Quantitative Susceptibility Mapping (QSM), and Diffusion Tensor Imaging (DTI). Typical functional imaging methods include Blood Oxygen Level-Dependent functional MRI (BOLD-fMRI), MR Thermometry (MRT), and MR Elastography (MRE). Metabolic imaging methods include MR Spectroscopic Imaging (MRSI) and, more recently, Spectroscopic Imaging by exploiting spatiospectral CorrElation (SPICE) [164, 179]. When selecting specific imaging sequences, spatial resolution, temporal resolution, SNR, artifacts, and reconstruction speed are primary considerations [180]. For preoperative diagnosis and planning, spatial resolution and SNR have a higher priority than temporal resolution. Conversely, for intraoperative MRI, temporal resolution and latency time have a higher priority than spatial resolution. Although the requirement for spatial resolution is not as high as that for diagnosis or planning purposes, it has to be higher or at least comparable to the precision achievable by the surgical robot and/or the precision required for a particular type of intervention. For example, in DBS surgery, a spatial resolution of ~ 1 mm and a temporal resolution of ~ 1 s are acceptable before approaching the target nucleus. If the target nuclei are smaller than 1 mm, a spatial resolution of < 1 mm is desired when approaching the target for fine positioning. At this stage, the spatial resolution outweighs temporal resolution, allowing the surgeon to sacrifice scan time for better positioning. However, for brain tumor biopsy, if the size of the tumor is > 10 mm, a spatial resolution of 1 ~ 2 mm and a temporal resolution of ~ 1 s are sufficient.

In robot-assisted surgery, MR imaging can be performed before, during, and after the surgery for planning, guidance, and evaluation. Preoperative MRI is usually carried out for diagnosis, lesion localization, and surgical planning. A typical workflow for robotic-assisted treatment planning includes [168, 181–183]: 1) embedding an MR visible fiducial marker/frame in the robot; 2) 2D/3D MR imaging of the subject and the robot with a high spatial resolution [11, 173]; 3) registering the CAD model of the robot and a rendering of the robot's reachable workspace to the 3D anatomical MR images; 4) trajectory planning [184]. Anatomical T1W and T2W imaging are mostly used for preoperative MRI [11, 173]. In MRI-guided robotic systems with intraoperative MRI, synchronous imaging ("interactive/real-time MRI") is performed along with remote-controlled intervention. Anatomical imaging [22, 44, 167] and thermometry imaging [11, 172, 173] are used for intraoperative MRI. During the treatment, fast imaging is desired, thus 2D imaging using sequences such as GRE [17, 22, 169], FLASH [19],

Table 5 Intraoperative MRI in robot-assisted surgery

Surgery	MR modality	Subject	MR scanner (Inc.)	2D/3D imaging	Sequence TR/TE (ms)	Spatial resolution (mm^3)	Temporal resolution (s)	Interactive MRI	Refs
Cardiac intervention	Anatomy	Phantom	1.5 T (GE)	2D	3.9/1.168 (GRE)	Thickness 30 mm	0.2	Yes	Dong (2022) [22]
Neurosurgery	Anatomy	Cadaver	3 T	2D	12/1.72	1.4×1.4×4	1.5	Yes	Cheng (2021) [167]
Lower back pain injections	Anatomy	Phantom	1.5 T (Siemens)	2D	189.94/1.67	2×2×5	0.68	Yes	Li (2020) [168]
Needle placement	Anatomy	Phantom	3 T (Siemens)	2D	5.88/3.17 (GRE)	2.4×2.4×5	1.3	Yes	Mikaiel (2020) [169]
Neurosurgery	Anatomy	Phantom	1.5 T (GE)	2D	68/2.8 (FSPGR)	0.98×0.98 mm^2	17.4	Yes	Guo (2018) [44]
Breast biopsy	Anatomy	In vivo Animal (Pig)	3 T (Siemens)	2D	4.1/1.5 (FLASH)	1.56×1.56×3	0.4	Yes	Yang (2014) [19]
Prostate brachytherapy	Anatomy	Phantom	3 T (Philips)	2D	2/1 (SE-EPI)	FOV 240 mm Thickness 5 mm	0.4	Yes	Su (2011) [170]
Transrectal prostate biopsy	Anatomy	Human	3 T (Siemens)	2D	8.94/2.3 (bSSFP)	1.56×1.56×5	0.9	Yes	Yakar (2011) [171]
Transperineal prostate intervention	Anatomy	Human	1.5 T (Philips)	3D (2 slices)	5.7/2.8 (bSSFP)	1.3×1.3×10	5.2	Yes	Bosch (2010) [13]
Transoral laser microsurgery	Thermometry	Cadaver	3 T (Philips)	3D (14 slices)	15/5 (FSE)	0.48×0.48×2	20	Yes	Fang (2021) [11]
Transrectal prostate cancer therapy	Thermometry	In vivo Animal (Rabbit)	1.5 T (GE)	2D	80/25.5 (EPI)	2.34×2.34×2	1	Yes	Giannakou (2021) [172]
Neuroablation	Thermometry	Animal (Swine)	3 T (Philips)	2D	39/15 (FFE-EPI)	1.39×1.39×7	2.78	Yes	Patel (2020) [173]
Neuroablation	Thermometry	Human	1.5 T (Siemens)	3D (3 slices)	81/19.1 (GRE)	2×2×5	7.8	Yes	Sloan (2013) [17]

FOV Field of View

Interactive MRI: simultaneous MR scanning and robotic surgery within the MR bore

Sequence: ***GRE*** GRadient Echo, ***FIESTA*** Fast Imaging Employing STeady-state Acquisition, ***FSPGR*** Fast SPoiled Gradient-Recalled echo; ***FLASH*** Fast Low Angle SHot, ***EPI*** Echo-Planar Imaging, ***SE-EPI*** Spin-Echo EPI, ***bSSFP*** balanced Steady-State Free Procession, ***FSE*** Fast Spin Echo, ***FFE-EPI*** Fast Field Echo EPI

EPI [170, 172], and bSSFP [13, 171] are commonly applied. In scenarios where 3D imaging is required, multi-slice 2D imaging is employed [11, 13, 17]. Postoperative imaging is typically carried out to evaluate surgical outcomes. Since there is no requirement for temporal resolution, conventional sequences can be used. For example, Yakar et al.used a T2W true fast imaging with steady-state precession sequence in the axial direction after a transrectal prostate biopsy surgery to measure the biopsy depth [171].

Efficient k-space coverage

Conventional MR imaging takes a relatively longer time than CT or X-ray because the image acquisition in k-space is done in a step-by-step Cartesian sampling manner. This line-by-line sampling requires signal excitation and acquisition for each Cartesian line. Therefore, Echo Planar Imaging (EPI) accelerates imaging by acquiring multiple Cartesian lines with a single excitation [185].

Acquisition of k-space using non-Cartesian trajectories, such as spiral and radial sampling, can also accelerate imaging. These sampling techniques are becoming popular for real-time MRI due to their motion robustness and tolerance to undersampling [180]. Early fast imaging methods for intervention also used data-sharing schemes such as keyhole and sliding-window methods [186]. The aforementioned non-Cartesian sampling scheme combined with advanced reconstruction methods can achieve high acceleration rates [187, 188]. All of these sampling schemes are suitable for both 2D and 3D imaging. For example, radial or spiral can be easily extended to 3D stack-of-stars or 3D stack-of-spiral by adding phase encoding steps along the kz direction [189]. In addition, 3D kooshball patterns have also been developed to provide isotropic FOV and spatial resolution [190].

Parallel imaging and coil arrays

Parallel imaging with coil arrays is one of the earliest explored methods for fast MR imaging. Multiple coils that can simultaneously receive signals from the imaging target reduce the burden of full k-space acquisition. By skipping k-space lines, partially sampled k-space reduces the image acquisition time. Coil sensitivity information helps provide the information for image recovery [191]. Two primary parallel imaging methods have been developed: SENSitivity Encoding(SENSE) [192] and GeneRalized Autocalibrating Partially Parallel Acquisitions (GRAPPA) [193]. SENSE reconstructs images in the image domain while GRAPPA does so in the Fourier domain. Both SENSE and GRAPPA are available with modern vendor-supplied reconstruction platforms. Many reconstruction algorithms have been developed based on extensions, combinations, and modifications of SENSE and GRAPPA. For example, SPIRiT (iTerative Self-consistent Parallel Imaging Reconstruction) [194] and its eigenvector-based implementation (ESPIRiT) [195] combine key features of SENSE and GRAPPA. SPIRiT is a coil-by-coil autocalibration method based on GRAPPA and its reconstruction is formulated as an inverse problem like SENSE. ESPIRiT uses an eigenvector decomposition to compute coil sensitivity maps for a generalized SENSE reconstruction. The implementation of parallel imaging in non-Cartesian sampling is also explored [196]. Coil selection [197] and array compression [198] are also used to accelerate reconstruction.

Advanced reconstruction techniques

Parallel imaging typically provides 2–4 times the acceleration rates [180]. By itself, it is not sufficient for interactive/real-time MRI-guided robotic intervention. Many fast reconstruction techniques based on undersampled K-space data have been developed to achieve high-fold acceleration. Early methods include constrained reconstruction [199], Generalized Series (GS) model [200, 201], and k-t methods such as UNFOLD [202] and k-t BLAST/SENSE [203]. Since the introduction of Compressed Sensing (CS) by Lustig et al. [204], CS-based methods have become popular in the past decade [205]. Combined with k-t methods, k-t FOCUSS [206], Golden-angle Radial Sparse Parallel MRI (GRASP) [207] were proposed for dynamic MRI. Liang et al. have proposed Partially Separable Functions (PSF) for spatiotemporal imaging [208] and high-dimensional imaging [209]. With joint partial separability and sparsity constraints, k-t Sparse and Low Rank Approach (k-t SLR) and similar works [210] have been proposed for dynamic MRI [211]. Using a low-rank plus sparse decomposition scheme, k-t Robust Principal Component Analysis (k-t RPCA) [212] and L + S methods [213] were applied to dynamic imaging and extended to temperature imaging [214]. He et al. developed a low-rank and framelet-based sparsity decomposition algorithm for brain interventional MRI [215]. Notably, a non-linear inverse reconstruction (NLINV) method has been used for real-time cardiovascular MRI-guided endomyocardial biopsies [216].

Recently, the use of deep learning for fast MRI has attracted extensive interest [217–221]. Deep learning-based methods can be roughly classified into two types: data-driven end-to-end methods (*e.g.*, AUTOMAP [222], U-Net [187], RNN [223], and DAGAN [224]) and physics-based unrolling methods (*e.g.*, DCCNN [225], ADMM-CSNet [226], ISTA-Net [227], SLR-Net [228], and L + S-Net [229]). Data-driven methods can reconstruct images rapidly and have been used for real-time MRI. For example, Zufiria et al.proposed a feature-based convolutional neural network for the reconstruction of interventional MRI [230]. Jaubert et al.developed a deep artifact suppression using recurrent U-Nets for real-time cardiac MRI [187]. A similar deep learning-based reconstruction with radial sampling has also been proposed for real-time MRI-guided radiotherapy [231]. Compared to data-driven methods, physics-based unrolling methods have better generalizability and interpretability. For example, an unrolled variational network with an undersampled spiral k-space trajectory was also used for real-time cardiac MRI reconstruction [188]. Recently, many novel deep learning techniques, such as self-supervised learning [232], unsupervised learning [233], transformers [234], and diffusion models [235], have also been applied to accelerate MR imaging.

For interactive/real-time MRI-guided robotic intervention, low-latency reconstruction is of great importance. The iterative reconstruction algorithms mentioned above, such as CS-based methods, are usually computationally expensive.

The deep learning-based methods, especially unrolled networks based on the physical model, can achieve a reconstruction time of milliseconds. Future endeavors in this field are expected to produce more improved deep learning-based algorithms for on-line reconstruction. In addition, with the development of more advanced deep learning hardware architectures and improved Graphics Processing Units (GPU) [236, 237], faster implementation of the algorithm are expected to further increase the speed. Combination of physics-driven deep-learning algorithm, combined with large-scale parallel processing are expected for improved MRI-guided surgery.

Intraoperative guidance and visualization

Segmentation of preoperative MR images is necessary to localize the target tissue for treatment planning. Deep learning-based segmentation algorithms have become state-of-the-art [238]. Several open-source 3D segmentation software tools can be used, *e.g.*, for pelvic surgery planning [239]. A Graphic User Interface (GUI) is usually developed for treatment planning and visualization. For example, Tavakkolmoghaddam et al. developed a surgical planning toolkit for an MR conditional stereotactic neurosurgery robot [240]. This toolkit streamlines the current surgical workflow by rendering and overlaying the robot's reachable workspace on the MRI image. It also helps identify the optimal entry point by segmenting the cranial burr hole volume and locating its center. For intraoperative guidance, dynamic shape instantiation has been developed [241, 242]. These methods use limited planar views of the imaging data combined with statistical shape information to provide real-time 3D reconstruction, thus further improving the performance of intraoperative guidance. In addition, automatic target segmentation and localization during surgery could aid in the closed-loop control of MRI-guided robots. Deep learning-based automatic needle segmentation and tracking have been applied to MRI-guided prostate biopsy [243] and percutaneous interventions [244]. A mechatronic system was also proposed to enable real-time control of MRI-guided instruments in the presence of respiration-induced target motion [245].

MRI-guided robot intervention systems

In this section, we provide further details on some of the exemplar MRI-guided surgical robots being developed or used in different clinical specialties, as shown in Fig. 7 and Table 6. From a detailed analysis of the functionality of these systems, new insights can be derived in terms of meeting the clinical demands for early and precision intervention, as well as the emerging technological challenges to be addressed in developing systems with higher DoFs and operational accuracy.

Table 6 Exemplar MRI-guided robotic systems and their actuation schemes, accuracy and the development state that they are in

Surgical Scenario	Actuation	Application	Accuracy	Mechanism	Status*	Ref
Brain	SMA/Tendon	Tumor removal	1.33%	6-DoF	P	Wang (2018) [16]
	Piezo	LITT	Submillimeter	2-DoF	F	Sloan (2013) [17, 174]
	Piezo	Stereotaxic and microsurgery	Submillimeter	8-DoF	F	Lang (2011) [5, 175]
	Piezo	DBS	1.45 ± 0.66 mm	8-DoF	P	Li (2021) [18]
Prostate	Piezo	Biopsy	4 mm	4-DoF	H	Patel (2019) [12, 176]
	Pneumatic	Biopsy	2.55 mm	6-DoF	F	Stoianovici (2017) [7, 177]
	Pneumatic	Brachytherapy and biopsy	NA	5-DoF	H	Bosch (2010) [13]
	Pneumatic	Biopsy	5.7 mm	5-DoF	F	Bomers (2017) [14, 178]
	Piezo	Biopsy	2.4 mm	4-DoF	A	Moreira (2021) [15]
Artery	Pneumatic	PCI	3.1 mm	4-DoF	A	Dagnino (2022) [8]
	Hydraulic	Electrophysiology	1.53 mm	3-DoF	P	Dong (2022) [22]
	Pneumatic	TAVR	1.14 ± 0.33 mm	8-DoF	A	Chan (2016) [23]
	Piezo	PCI	0.1 mm $7 \pm 6°$	3-DoF	A	Tavallaei (2016) [20]
Breast	Piezo	Biopsy	2.5 mm	3-DoF	H	Pfleiderer (2005) [6]
	Piezo	Biopsy	10 mm	6-DoF	A	Yang (2014) [19]
Spinal cord	Piezo	Cannula alignment	2.57 ± 1.09 mm	4-DoF	P	Li (2022) [10]
	Pneumatic	Cellular therapeutics	0.48 mm	2-DoF	P	Squires (2021) [25]
Liver	Pneumatic	Laser ablation	2.5 mm	4-DoF	H	Franco (2016) [9]
Oral	Hydraulic	Laser ablation	0.2 mm	5-DoF	P	Fang (2021) [11]
MRgFUS	Piezo	MRgFUS	NA	4-DoF	P	Antoniou (2022) [24]

**P* Phantom study/Ex vivo/Cadaver, *A* Animal study, *H* Human study, *F* FDA clearance

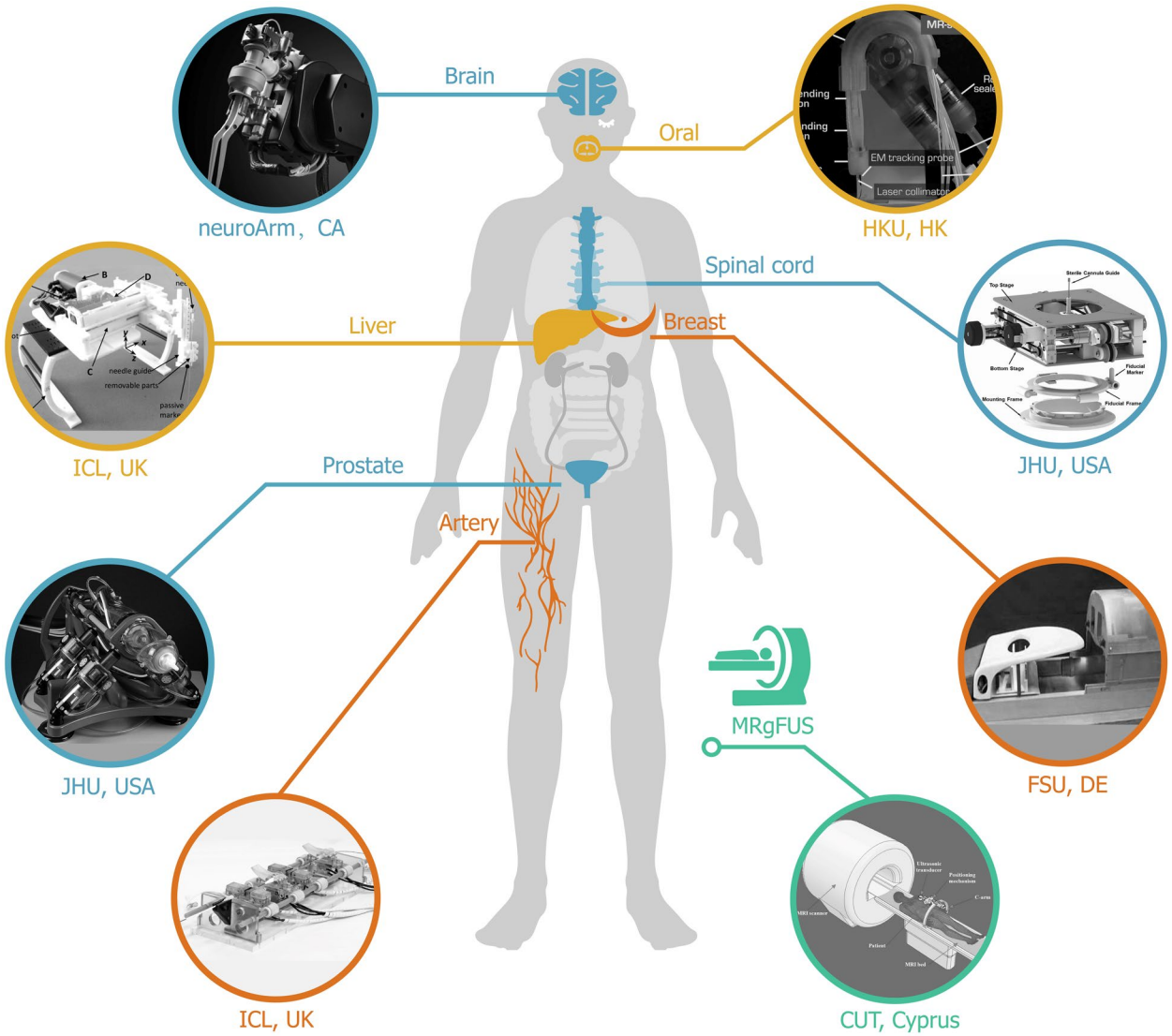

Fig. 7 Exemplar MRI-guided robotic systems for various clinical applications, showing example systems for: neuroArm for brain surgery developed by University of Calgary [246]; MrBot for prostate biopsy developed by Johns Hopkins University [7]; Imperial College London's system for artery intervention [8]; ROBITOM II for breast surgery developed by Friedrich Schiller University Jena [6]; The University of Hong Kong's system for transoral surgery [11]; Johns Hopkins University's system for spinal cord treatment [10]; Imperial College London's system for liver ablation [9] and Cyprus University of Technology's system for MRgFUS [24]

a) Brain

MRI-guided robots are used in a variety of brain surgery procedures, including electrode implantation, laser and radiation surgery, thermal ablation, and biopsy. MRI is particularly suitable for neurosurgery as it provides clear contrast for soft tissues. The neuroArm robot, one of the most prominent MRI-guided robots, has a piezo actuated due arm configuration for stereotaxic and microsurgery [246]. The integrated sensing system provides effective visual and haptic feedback, which can be adapted to different clinical scenarios. NeuroArm also provides motion scaling and Z lock features to ensure straight-line motion toward the target even if the operator motion deviates from the path. In the first 35 clinical studies, the system achieved a speed of 200 mm/and 1 mm position accuracy with a payload of 500 g.

b) Prostate

Prostate intervention is one of the focused research areas in MRI-guided robotics. The current gold standard approach for prostate biopsy is transrectal ultrasound (TRUS) guidance, which doesn't always provide clear enough tissue visualization. MRI guided robots have the advantage of enabling automatic targeting by using high contrast images. MrBot claims to be the first FDA-approved MR-safe robot for prostate biopsy [7]. It has a 6-DoF hybrid tracking system where 5-DoF is based

on a parallel positioning structure and another 1-DoF for needle insertion actuated by a pneumatic motor [37]. Optical fibers are used for position feedback and marker registration. Clinical experiments on five patients show an average of 30 min completion time and a targeting accuracy of 2.55 mm.

c) Artery

For endovascular intervention, MR-conditional guidewires and catheters are used. The Hamlyn Centre for Robotic Surgery at Imperial College London, UK, developed an advanced teleoperated robotic system that provides an intuitive user interface [8]. The patient-side robot uses guide wheels capable of manipulating conventional catheters and guidewires in standard MR environment. Its manipulator is pneumatically actuated and manufactured with polymer materials. Hence the interference for MR imaging is negligible. A small scale surgical study showed a 100% success rate of precisely accessing five target arteries [8].

d) Breast

Mammography X-ray remains the de facto standard for breast cancer detection despite its technical drawbacks. In meeting the clinical demand of precision surgery, MRI robots are showing promises of enabling simultaneous imaging and intervention. Several iterations of ROBITOM prototypes have been developed. ROBITOM II is equipped with a dedicated double breast coil and a high-speed trocar setting unit [247]. Four patients with MR-detectable breast lesions underwent biopsy procedures. Specimens were harvested with a coaxial technique by using a 14-G core needle biopsy gun under 1.5 T whole body scanner [6].

e) Oral

Transoral laser microsurgery is a solution for treating early-stage glottic cancers. The utilization of highly localized laser beams enables precise tissue incision with minimal thermal spread to the surrounding healthy tissues. The advantage of using MR imaging for laser microsurgery is the thermal distribution during incision can be monitored simultaneously. Fang et al. [11] proposed an MRI-guided soft robotic manipulator for MRI-guided transoral laser microsurgery. A small 12×100 mm robotic system was designed to adapt to a curved oral cavity. The two soft segments, each composed of three elastomer chambers, could be individually adjusted by microvolume (< 0.004 mL) valves. The hydraulic power was transmitted by leader–follower units. A data-driven learning method was used to implement path-following ablation tasks. A mean error of 0.2 mm was achieved.

f) Spinal cord

Low back pain is a common problem in adults, which can be caused by arthritis, structural problems and disk injuries, as well as strain/injury to muscles or tendons in the back. Pain relief can be achieved through medication, physical therapy and rest. For interventional treatment, image-guided therapeutic facet joint steroid injection is a common procedure. Li et al. [10] from Johns Hopkins University developed an MR conditional body-mounted robot to allow interventional radiologists to position and manipulate the spinal surgery needle. The 6-DoF robot was composed of a 4-DoF needle alignment module and a 2-DoF remotely actuated needle insertion module. The system circumvented the need to move the patient in and out of the scanner during a procedure. A dedicated clinical workflow was proposed for robot-assisted lower back pain injections under real-time MRI guidance. A phantom study demonstrated a mean absolute tip position error of 1.50 ± 0.68 mm and needle angular error of $1.56 \pm 0.93°$.

g) Liver

Percutaneous laser ablation utilizes a water-cooled end effector to deliver thermal energy generated by a high-power laser source directly to the liver lesion, allowing the treatment of otherwise inoperable liver tumors. Manually placing the catheter can be time consuming, requiring comprehensive training. MRI-guided robotic procedure is time efficient and provides in situ, in vivo thermal monitoring. Franco et al. proposed a 4-DoF (PPRR) robot for liver ablation [9]. Two pneumatic actuators were arranged in parallel, and two others were arranged in series to make a multi-modal serial-parallel manipulator. Consecutive actuation of actuators enabled translation, while additional actuators resulted in rotation. A novel time-delay control scheme was also proposed without the need of position or force feedback for pneumatic control. The targeting error was less than 5 mm, and an SNR loss under 5% was reported. Human studies showed the robot could save surgical time by up to 30 min for each lesion.

h) MRgFUS

The non-invasive nature of Focused Ultrasound (FUS) therapy, augmented with increased accuracy robotic guidance, presents promising clinical potential. Antoniou et al. [24] developed a robotic system for MRgFUS therapy of tumors in the breast, bone, thyroid, and abdomen. A special C-shaped structure was designed to be attached to the table of conventional MRI systems. Four motion stages were fixed to the C-arm. Each stage was dedicated to positioning a 2.75 MHz spherically focused transducer relative to a patient in the supine position. MR compatibility and RF heating safety were evaluated using agar-based phantoms showing no significant SNR losses.

Discussion and future outlook

Compared to general surgical robots, the development of MRI-guided systems is still in its infancy. Whilst the concept itself has been proposed for many years, its engineering

development and clinical adoption remain slow. With increasing drive for early intervention and precision surgery, underpinned by recent advances in MR hardware and fast imaging techniques, this trend is likely to be changed. There are already national initiatives in developing new generation, integrated theranostic systems based on MRI guidance and the pace of new development in this area is likely to accelerate in the next 5–10 years. Before we see rapid uptake of these systems clinically, the following research and engineering challenges need to be addressed.

Actuation and sensing

Physical separation between the MR scanner and control room (> 6 m) poses a challenge for remote actuation of the MRI-guided surgical robots. The distance can lead to low control frequency (usually < 20 Hz) for the pneumatic, hydraulic, and cable-driven motors due to hysteresis. The physical separation also poses challenges to minimizing the size of the mechanical transmission. For consideration of MR safety, components made of nonmetallic materials are used. Although these components can be 3D printed, they suffer from relatively weak mechanical properties. If piezoelectric actuation is used for high-precision control, it may cause a high SNR loss. Due to the limited size of the MR bore (usually < 70 cm), the allowable size of the robot and actuators is also limited. The size limitation could further compromise its mechanical performance. Distance between the actuator and the controller also poses challenges for sensing. As we further miniaturize the size of the robot and interventional devices, their integration with sensors can be difficult. In addition, signal shielding is usually required, which adds additional constraints. Future developments in MR-safe actuation and sensing include: 1) direct actuation methods with short transmission link and compact designs; 2) novel mechanical designs based on new materials and fabrication schemes; 3) self-shielding materials and embodiment schemes; 4) multi actuation methods and hybrid actuation designs; 5) smart materials with integrated sensing, actuation and localization.

Materials

The main challenges of material selections for MRI-guided Robots include: 1) A lack of database and reference designs for research and development of MR conditional materials. Thus far, no mature material system has been used commercially. 2) Limited knowledge of the design processes. The dependence of microstructure on electromagnetic properties has not been systematically investigated in the literature. It is difficult to optimize the magnetic susceptibility and MRI artifacts by microstructure control through ad hoc processing and heat treatments. 3) Balance between electromagnetic and mechanical properties. The electromagnetic and mechanical properties are significantly dependent on the microstructure (phase composition and distribution, texture, grain size, etc.). The optimal microstructure for the electromagnetic property would compromise the mechanical performance. For instance, the increase of ω phase can minimize the magnetic susceptibility but cause a brittle fracture in Zr–Nb alloys. 4) Formability and machinability. Adequate sharpening combined with sufficient elasticity is challenging. For instance, surface control and machining of shape thin-wall needles with small diameters for interventional devices are difficult to carry out, especially in ceramics and plastics, due to their poor stiffness and hardness.

Future developments of materials for MRI-guided Robots include: 1) Microstructure control—it is necessary to systematically build the relationship between microstructure and electromagnetic performance in different material systems and to balance the electromagnetic and mechanical properties, as well as the biocompatibility. 2) Explore the composite structure containing metals, polymer and/or ceramic. Metals, such as β Ti-Zr-based alloys composed of biocompatible alloying elements, have high mechanical performance and good machinability with the main drawback of MR compatibility, whereas ceramics or polymers can complete the requirement. 3) Improvement of fabrication method—apart from conventional fabrication methods, additive manufacturing is a reliable alternative technique to fabricate components in complex geometries and with a high possibility of producing functionally graded or multi-material components.

Interventional instrument

Among the many ablation procedures, RF is the most commonly used technique in current clinical practice. However, RF cannot be accurately focused and it can create excessive and irregular heating of the superficial tissues. Microwaves provide improved performance than RF but are associated with significant temperature gradients, which may result in adverse consequences. It also has a significant loss of tissue penetration at frequencies above 1000 MHz. HIFU also has restricted thermal penetration [151]. LITT is usually used for treating lesions with a relatively small size. Most reported LITT studies on gliomas comprised lesions of < 10 cm^3 (~ a radius of 1.33 cm). Treatment of larger neoplasms using LITT carries a high risk of brain edema [151]. iMRgFUS can treat relatively large target volume, but existing studies showed that the predicted lesion size for postmortem sections generally did not correlate with imaging and surgical planning [126]. Similar problems also exist for cryoablation [125]. The precise control of the treatment volume still needs to be tackled.

General challenges for the intervention instruments include: 1) Limited understanding of in vivo deflection mechanisms. Almost all interventional devices cannot be actively controlled for directing the tips or probes. This limits the application scenarios and flexibility of the devices, *e.g.*, in cardiac intervention [248]. 2) MR image artifacts—the artifacts produced by the interventional devices vary. Although efforts have been taken to reduce device-specific artifacts [104], this remains a challenge. 3) RF-induced heating—during MR imaging, RF waves with a frequency between several tens to several hundreds of MHz are sent to the scanner. The intervention device, as well as the surrounding tissue, can be heated up. Although commercial devices were tested for the heating effect [249], RF heating still poses a great challenge to the development of new devices and procedures. In addition, since interventional procedures are carried out in an MR scanner, all instrumentations that go with the interventional devices must be MR conditional. This could bring additional costs to the surgical procedure.

Future development of MR-safe or MR-conditional interventional devices include: 1) flexible and interchangeable devices for MRI-guided robots. The devices have to be able to fit a variety of different robot platforms for installation and detachment. 2) Improved compatibility with the MR imaging system. MR image guidance requires coordinate transformation between the image and robot coordinates. Therefore, interventional devices need to be easily fitted to the robot operating system. 3) Improved combability with the MR coils and operating space—this is especially important for neurosurgery since the head coil usually has limited space. 4) Integration of the actuator and sensors—smart devices that are embedded with actuation and sensing functions can greatly improve the consistency and accuracy of the surgical operation. 5) Multi-functionality—so far, most interventional devices have only one-single function. For example, the catheter guidewire may also be used as a guide for biopsy or LITT, thus facilitating more flexibility and integration during MRI-guided intervention.

Interactive/real-time MRI

Many advanced MRI techniques have been developed over the past decades. However, only limited methods have been integrated into MRI guided robots. The challenges of MRI for robotic surgery include: 1) Limited MRI modalities used in interactive guidance. New MR imaging modalities such as DTI [250], QSM [251], BOLD-fMRI [252], MRE [253], and MRSI [254] have been used in conventional surgery, but only a few MR modalities (mainly anatomical and thermometry imaging methods) are used in MRI guided intervention. Limited information may affect the outcome of robotic surgery. 2) Low spatiotemporal resolution of interactive/real-time MRI. Interactive/real-time MRI with low spatiotemporal resolution and SNR is available in some MRI guided robotic systems. To further improve the accuracy of treatment, 2D/3D intraoperative imaging with high spatiotemporal resolution and SNR of MRI is the prerequisite of future MRI-guided intervention robot systems. 3) Motion and instrument-induced MRI artifacts. MRI artifacts induced by the patient's motion and metallic instruments and implants could infer the images. Although optimized or specialized sequences could help to reduce the artifacts [255], this problem still needs a general and efficient solution.

Future directions for MRI in robotic intervention include: 1) Rich, multimodal preoperative information for the surgery—more imaging pulse sequences (*e.g.*, anatomical, functional, and metabolic) or multimodal imaging techniques (*e.g.*, MR fingerprinting (MRF)) could be added to the preoperative protocols to provide adequate information for robotic surgery. 2) Artificial Intelligence (AI)-assisted MRI. Machine learning and deep learning-enabled MRI technologies have shown promising applications to image reconstruction, segmentation, and categorization. Steady progress is expected in improving the spatiotemporal resolution and SNR of interactive/real-time MRI. In addition to image reconstruction, AI-based methods can facilitate real-time interventional imaging and processing including feature recognition and tracking, on-line quantitative evaluation and treatment response assessment, as well as autonomous interventional navigation. These could help improve the overall autonomous level of the MRI-guided robots [256]. 3) Application of low-field (< 0.5 T) and ultra-low-field (< 0.1 T) MRI [257–259]. The low-field MRI systems have natural advantages for MRI-guided intervention due to their more relaxed requirement and tolerance for MR compatibility of surgical tools in terms of image distortion and artifacts. In addition, the low cost and high portability of the low-field MRI could enable a wider application of MRI-guided surgical robots in wider clinical scenarios, even for out-patient screening and minimally invasive intervention.

MRI-guided surgical robots

Most of the MRI-guided robotic systems thus far are for surgical procedures of prostate, brain, breast, and artery. Based on the 95 independent systems, 24% of them were for prostate surgery, 14% for brain surgery, 14% for breast surgery, 9% for artery, 7% for liver surgery, 5% for MRg-FUS, 4% for spinal cord surgery and 23% for others. Recently, robot for oral intervention was also proposed. Although MRI-guided robotic systems are hot topics for research, only a handful of robots were in the process of clinical translation.

The main challenges in translation to clinical surgery include: 1) Gap between interventional needs and system development—there is a mismatch between the development of fully MR-safe mechatronics and clinical consideration of viable surgical workflows. These features could be missing teleoperated control, poor user interface design, lack of perceptual (*e.g.*, haptic or tactile feedback) and MR conditional, high-performance actuators. 2) Efficiency of operation—since MRI can be more expensive as compared to other imaging modalities, minimizing the time of the procedure in the MRI room is critical for the realization of this technology. 3) Interactive feedback—most of the aforementioned robotic surgeries are based on 2D imaging. A major challenge remains for 3D real-time imaging, which is crucial for visual feedback. The image-guided haptic guidance is limited to 2D imaging, whereas the use of 3D real-time guidance is promising for the effectiveness, precision, and safety of surgery. 4) System miniaturization and cost reduction—while some hospitals have specialized interventional MRI suites, there is a major benefit to developing robots that are capable of operating in existing MRI scanners. Thus, there is a commercial benefit in building compact, application specific, MRI scanner fitted robotic systems. There could be great benefits to having robots that can be readily and quickly deployed to standard diagnostic MRI scanners without compromising hospital workflows. Future directions of developing robotic systems include: 1) Ease of integration with the clinical scanner for imaging and guidance. 2) Safe and effective actuation and sensing approach incorporated into the system design. 3) Application of high-quality real-time imaging for precision, safe, effective surgeries. 4) Full integration of robot design with MR scanners with more open access, and ideally mobile system without the need of specialized shielding and can be deployed to standard operating theatres.

Operating room for robot-assisted surgeries

Clinically, an ideal, futuristic operating room needs to integrate advanced imaging technologies, robotic systems, and supporting equipment all in one. This can provide a platform to support both research and development of new minimal intervention procedures aimed at precision intervention and personalized treatments. An exemplar integrated operating suite is the Advanced Multimodality Image Guided Operating Suite (AMIGO), which includes three rooms with a 3 Tesla MRI room, an operating room (OR), and a PET/CT room. It provides different imaging modalities before, during, and after surgery and has successfully promoted a variety of new surgeries. To integrate a robotic system with a future operating room, it is necessary to consider not only multimodal imaging technologies like the AMIGO system but also robot specific operating constraints, as well as the mobility, portability, and ergonomics considerations.

Mobile or portable, OR-compatible robotic systems

An operating room should be capable of accommodating the robotic system and its affiliated units, ensuring easy mobility and portable operation. For instance, a pneumatic or hydraulic actuation unit is used for MR-safe operation, but they carry long and tortuous transmission tubes connected to the robotic system. It can interfere with robotic movement or increases the payload of the robotic system. An integrated and embodied design of pneumatic or hydraulic transmission lines fully integrated with the operating room. Hence, a fundamental re-consideration of function integration is necessary at the beginning of infrastructure construction.

Multimodal imaging systems

Multimodal imaging is essential for precision intervention. They have already been integrated with platforms such as AMIGO. Future multimodal imaging systems need to provide cross-scale imaging information from macro to micro-levels (*e.g.* microcells and cellular information). They are particularly useful for assessing both system level and local level impact of the applied therapeutic procedures. Information concerning microcirculation, compound composition, energy metabolism, and oxygen content are all relevant. There is a real-opportunity in integrating MR-safe continuum robot integrated with biphotonic probes and focused energy delivery methods.

Integrated OR-compatible life-supporting equipment

For effective MRI-guided intraoperative robotic surgery, MR-safe/conditional life-supporting equipment is essential to guarantee life maintenance during the surgery. It includes MR-safe/conditional vital sign monitoring devices, anesthesia respirator, syringe pump and power injectors. All equipment needs to work intraoperatively to continuously provide life support without interfering with the imaging and robot operation processes. In this regard, effective shielding and stringent EMC constraints are essential.

Test and regulations

Functional tests and performance tests are essential for MRI-guided robotic system development, including compatibility, distortion, safety, SNR, DoF, payload capability, absolute positioning accuracy, and repeated positioning accuracy. Table 7 outlines the key consideration of different standards that need to be followed in developing MRI-guided surgical robot systems.

Table 7 Test requirement and regulation standards to be followed for developing MRI-guided robotic systems

Items	Index	Standard No	Standard Name
Functional test	Safety	ASTM F2503	Standard Practice for Marking Medical Devices and Other Items for Safety in the Magnetic Resonance Environment
		ASTM F2213	Standard Test Method for Measurement of Magnetically Induced Torque on Medical Devices in the Magnetic Resonance Environment
		ASTM F2182	Standard Test Method for Measurement of Radio Frequency Induced Heating On or Near Passive Implants During Magnetic Resonance Imaging
		ISO/TS 10,974	Assessment of the Safety of Magnetic Resonance Imaging for Patients with an Active Implantable Medical Device
Performance test	SNR	NEMA Standards Publication MS 1–2008 (R2014)	Determination of Signal-to-Noise Ratio in Diagnostic Magnetic Resonance Imaging
	Absolute positioning accuracy	ASTM F2052	Standard Test Method for Measurement
	Repeated positioning accuracy	ASTM F2052	Standard Test Method for Measurement
Human study	Clinical diagnostic	F2978-20	Standards Guide to Optimize Scan Sequences for Clinical Diagnostic Evaluation of Metal-on-Metal Hip Arthroplasty Devices using Magnetic Resonance Imaging

Conclusions

MRI-guided robot intervention is a promising technique that has broad application values because of its safety, versatility, and true theranostic potential. Technically, significant achievements have been made in areas such as actuation, sensing, new materials, interventional instruments, and interactive/real-time MRI. By combining novel sensor and actuator designs with advanced MRI sequences, new clinical breakthroughs are expected. New developments in MR-safe or conditional materials would encompass microstructure control, exploring the composite structure containing metals, polymer, and ceramic, and improving fabrication methods. Future development of MR conditional interventional instruments includes flexible and interchangeable instruments, improved compatibility with the MRI system itself and the robot, and multi-functional operation. For interactive/real-time MRI, leveraging rich preoperative information with AI-assisted reconstruction, image processing, and artifact suppression represents exciting future research directions. These technologies will require close collaboration among different disciplines. All these would contribute to our future pursuit of accurate, safe, multifunctional, and patient-specific therapies for the general population.

Supplementary Information The online version contains supplementary material available at https://doi.org/10.1007/s44258-023-00003-1.

Acknowledgements We thank Z. Zhang for providing detailed edits of all the figures in the paper and F. Xiao for the discussions of the outline and writing the first draft in the material section.

Authors' contributions All the authors contributed equally to this work.

Funding This work was supported in part by the National Key R&D Program of China (2022YFB4702700), the Science and Technology Commission of Shanghai Municipality (21DZ1100300) and the Science and Technology Commission of Shanghai Municipality (20DZ2220400).

Declarations

Competing interests The authors declare that they have no conflicts of interest. Author Guang-Zhong Yang is a member of the Advisory Board for Med-X. The paper was handled by another Editor and has undergone a rigorous peer review process. Author Guang-Zhong Yang was not involved in the journal's peer review of, or decisions related to, this manuscript.

References

1. Jolesz FA. Intraoperative imaging and image-guided therapy. Springer Science & Business Media; 2014.
2. Jolesz FA. Future perspectives for intraoperative MRI. Neurosurg Clin. 2005;16(1):201–13.
3. Su H, Kwok KW, Cleary K, Iordachita I, Cavusoglu MC, Desai JP, Fischer GS. State of the art and future opportunities in MRI-guided robot-assisted surgery and interventions. Proc IEEE. 2022;110(7):968–92.

4. Standard A. F2503. Standard practice for marking medical devices and other items for safety in the magnetic resonance environment. ASTM International; 2013.
5. Lang MJ, Greer AD, Sutherland GR. Intra-operative robotics: NeuroArm. Intraoperative Imaging: Springer; 2011. p. 231–6.
6. Pfleiderer SO, Marx C, Vagner J, Franke R-P, Reichenbach JR, Kaiser WA. Magnetic resonance-guided large-core breast biopsy inside a 1.5-T magnetic resonance scanner using an automatic system: in vitro experiments and preliminary clinical experience in four patients. Invest Radiol. 2005;40(7):458–63.
7. Stoianovici D, Kim C, Petrisor D, Jun C, Lim S, Ball MW, Ross A, Macura KJ, Allaf M. MR Safe Robot, FDA clearance, safety and feasibility prostate biopsy clinical trial. IEEE ASME Trans Mechatron. 2017;22(1):115–26.
8. Dagnino G, Kundrat D, Kwok TMY, Abdelaziz MEMK, Chi W, Nguyen A, Riga C, Yang GZ. In-vivo Validation of a Novel Robotic Platform for Endovascular Intervention. IEEE Trans Biomed Eng. 2023;70(6):1786-94.
9. Franco E, Ristic M, Rea M, Gedroyc WMW. Robot-assistant for MRI-guided liver ablation: a pilot study. Med Phys. 2016;43(10):5347–56.
10. Li G, Patel NA, Melzer A, Sharma K, Iordachita I, Cleary K. MRI-guided lumbar spinal injections with body-mounted robotic system: cadaver studies. Minim Invasive Ther Allied Technol. 2022;31(2):297–305.
11. Fang G, Chow MCK, Ho JDL, He Z, Wang K, Ng TC, Tsoi JKH, Chan PL, Chang HC, Chan DT, Liu YH, Holsinger FC, Chan JY, Kwok KW. Soft robotic manipulator for intraoperative MRI-guided transoral laser microsurgery. Sci Robot. 2021;6(57):eabg5575.
12. Patel NA, Li G, Shang W, Wartenberg M, Heffter T, Burdette EC, Iordachita I, Tokuda J, Hata N, Tempany CM. System integration and preliminary clinical evaluation of a robotic system for MRI-guided transperineal prostate biopsy. J Med Robot Res. 2019;4(02):1950001.
13. van den Bosch MR, Moman MR, van Vulpen M, Battermann JJ, Duiveman E, van Schelven LJ, de Leeuw H, Lagendijk JJW, Moerland MA. MRI-guided robotic system for transperineal prostate interventions: proof of principle. Phys Med Biol. 2010;55(5):N133–40.
14. Bomers J, Bosboom D, Tigelaar G, Sabisch J, Fütterer J, Yakar D. Feasibility of a 2nd generation MR-compatible manipulator for transrectal prostate biopsy guidance. Eur Radiol. 2017;27(4):1776–82.
15. Moreira P, Grimble J, Iftimia N, Bay CP, Tuncali K, Park J, Tokuda J. In vivo evaluation of angulated needle-guide template for MRI-guided transperineal prostate biopsy. Med Phys. 2021;48(5):2553–65.
16. Wang X, Cheng SS, Desai JP. Design, analysis, and evaluation of a remotely actuated MRI-compatible neurosurgical robot. IEEE Robot Autom Lett. 2018;3(3):2144–51.
17. Sloan AE, Ahluwalia MS, Valerio-Pascua J, Manjila S, Torchia MG, Jones SE, Sunshine JL, Phillips M, Griswold MA, Clampitt M, Brewer C, Jochum J, McGraw MV, Diorio D, Ditz G, Barnett GH. Results of the neuroblate system first-in-humans phase i clinical trial for recurrent glioblastoma: clinical article. J Neurosurg. 2013;118(6):1202–19.
18. Li G, Patel NA, Burdette EC, Pilitsis JG, Su H, Fischer GS. A fully actuated robotic assistant for MRI-guided precision conformal ablation of brain tumors. IEEE ASME Trans Mechatron. 2021;26(1):255–66.
19. Yang B, Roys S, Tan UX, Philip M, Richard H, Gullapalli R, Desai JP. Design, development, and evaluation of a master-slave surgical system for breast biopsy under continuous MRI. Int J Robot Res. 2014;33(4):616–30.
20. Tavallaei MA, Gelman D, Lavdas MK, Skanes AC, Jones DL, Bax JS, Drangova M. Design, development and evaluation of a compact telerobotic catheter navigation system. 2016;12(3):442–52.
21. Abdelaziz ME, Kundrat D, Pupillo M, Dagnino G, MY T, Kwok WC, Groenhuis V, Siepel FJ, Riga C, Stramigioli S, Yang G-Z. Toward a versatile robotic platform for fluoroscopy and MRI-guided endovascular interventions: a pre-clinical study. IEEE/RSJ International Conference on Intelligent Robots and Systems (IROS). 2019.
22. Dong ZY, Wang XM, Fang G, He ZL, Ho JDL, Cheung CL, Tang WL, Xie XC, Liang LY, Chang HC, Ching CK, Kwok KW. Shape tracking and feedback control of cardiac catheter using MRI-guided robotic platform-validation with pulmonary vein isolation simulator in MRI. IEEE Trans Robot. 2022;38(5):2781–98.
23. Chan JL, Mazilu D, Miller JG, Hunt T, Horvath KA, Li M. Robotic-assisted real-time MRI-guided TAVR: from system deployment to in vivo experiment in swine model. Int J Comput Assist Radiol Surg. 2016;11(10):1905–18.
24. Antoniou A, Giannakou M, Evripidou N, Stratis S, Pichardo S, Damianou C. Robotic system for top to bottom MRgFUS therapy of multiple cancer types. Int J Med Robot. 2022;18(2): e2364.
25. Squires A, Hovet S, Li R, Oshinski J, Ho Tse ZT. A body-mounted device for MRI-guided spinal therapy. Int J Med Robot. 2021;17(2): e2235.
26. Pappafotis N, Bejgerowski W, Gullapalli R, Simard JM, Gupta SK, Desai JP. Towards design and fabrication of a miniature mri-compatible robot for applications in neurosurgery. ASME international design engineering technical conferences and computers and information in engineering conference. 2008.
27. Monfaredi R, Cleary K, Sharma K. MRI robots for needle-based interventions: systems and technology. Ann Biomed Eng. 2018;46(10):1479–97.
28. Abdelaziz MEMK, Tian LBH, Hamady M, Yang GZ, Temelkuran B. X-ray to MR: the progress of flexible instruments for endovascular navigation. Prog Biomed Eng. 2021;3(3):032004.
29. Xiao Q, Monfaredi R, Musa M, Cleary K, Chen Y. MR-conditional actuations: a review. Ann Biomed Eng. 2020;48(12):2707–33.
30. Farooq MU, Ko SY. A decade of MRI compatible robots: systematic review. IEEE Trans Robot. 2022:1–23.
31. Tse ZTH, Elhawary H, Montesinos CF, Rea M, Young IR, Lampérth M. Testing MR image artifacts generated by engineering materials. Concepts Magn Reson Part B Magn Reson Eng. 2011;39:109–17.
32. Zhou D-B, Wang S-P, Wang S-G, Ai H-J, Xu J. Bulk metallic glasses: MRI compatibility and its correlation with magnetic susceptibility. J Mater Sci Technol. 2016;32(6):496–504.
33. Schenck JF. The role of magnetic susceptibility in magnetic resonance imaging: MRI magnetic compatibility of the first and second kinds. Med Phys. 1996;23(6):815–50.
34. Schaefers G, Melzer A. Devices and Materials in MRI. In: Kramme R, Hoffmann K-P, Pozos RS, editors. Springer Handbook of Medical Technology. Springer, Berlin Heidelberg: Berlin, Heidelberg; 2011. p. 503–21.
35. Ren Y, Li J, Wang Q, Yang K. A review: research on MR-compatible alloys in MRI. Acta Metall Sin. 2017;53(10):1323–30.
36. Hanawa T. Research and development of metals for medical devices based on clinical needs. Sci Technol Adv Mater. 2012;13(6): 064102.
37. Stoianovici D, Patriciu A, Petrisor D, Mazilu D, Kavoussi L. A new type of motor: pneumatic step motor. IEEE ASME Trans Mechatron. 2007;12(1):98–106.
38. Dong ZY, Guo ZY, Lee KH, Fang G, Tang WL, Chang HC, Chan DTM, Kwok KW. High-performance continuous hydraulic motor for mr safe robotic teleoperation. IEEE Robot Autom Lett. 2019;4(2):1964–71.

39. Liu W, Yang Z, Jiang S, Feng D, Zhang D. Design and implementation of a new cable-driven robot for MRI-guided breast biopsy. Int J Med Robot. 2020;16(2): e2063.
40. Ho M, Desai JP. Towards a MRI-compatible meso-scale SMA-actuated robot using PWM control. 3rd IEEE RAS & EMBS International Conference on Biomedical Robotics and Biomechatronics. 2010.
41. Vartholomeos P, Bergeles C, Qin L, Dupont PE. An MRI-powered and controlled actuator technology for tetherless robotic interventions. Int J Robot Res. 2013;32(13):1536–52.
42. Hofstetter LW, Hadley R, Merrill R, Pham H, Fine GC, Parker DL. MRI-compatible electromagnetic servomotor for image-guided medical robotics. Commun Eng. 2022;1(1):4.
43. Whitney JP, Chen T, Mars J, Hodgins JK. A hybrid hydrostatic transmission and human-safe haptic telepresence robot. IEEE international conference on robotics and automation (ICRA). 2016.
44. Guo ZY, Dong ZY, Lee KH, Cheung CL, Fu HC, Ho JDL, He HK, Poon WS, Chan DTM, Kwok KW. Compact design of a hydraulic driving robot for intraoperative MRI-guided bilateral stereotactic neurosurgery. IEEE Robot Autom Lett. 2018;3(3):2515–22.
45. Mutlu S, Yasa O, Erin O, Sitti M. Magnetic resonance imaging-compatible optically powered miniature wireless modular lorentz force actuators. Adv Sci. 2021;8(2):2002948.
46. Comber DB, Slightam JE, Gervasi VR, Neimat JS, Barth EJ. Design, additive manufacture, and control of a pneumatic. MR-Compatible Needle Driver IEEE Trans Robot. 2016;32(1):138–49.
47. Groenhuis V, Stramigioli S. Rapid prototyping high-performance MR safe pneumatic stepper motors. IEEE ASME Trans Mechatron. 2018;23(4):1843–53.
48. Groenhuis V, Siepel FJ, Stramigioli S. Magnetic resonance pneumatic stepper motor with multiple concentric shafts output. IEEE ASME Trans Mechatron. 2022;27(4):2379–89.
49. Farimani FS, Mojarradi M, Hekman E, Misra S. PneuAct-II: hybrid manufactured electromagnetically stealth pneumatic stepper actuator. IEEE Robot Autom Lett. 2020;5(2):3588–93.
50. Melzer A, Gutmann B, Remmele T, Wolf R, Lukoscheck A, Bock M, Bardenheuer H, Fischer H. INNOMOTION for percutaneous image-guided interventions: principles and evaluation of this MR- and CT-compatible robotic system. IEEE Eng Med Biol Mag. 2008;27(3):66–73.
51. Chen Y, Kwok KW, Tse ZT. An MR-conditional high-torque pneumatic stepper motor for MRI-guided and robot-assisted intervention. Ann Biomed Eng. 2014;42(9):1823–33.
52. Yang B, Tan UX, McMillan A, Gullapalli R, Desai JP. Design and control of a 1-DOF MRI compatible pneumatically actuated robot with long transmission lines. IEEE ASME Trans Mechatron. 2011;16(6):1040–8.
53. Chen Y, Godage IS, Tse ZTH, Webster RJ 3rd, Barth EJ. Characterization and control of a pneumatic motor for MR-conditional robotic applications. IEEE ASME Trans Mechatron. 2017;22(6):2780–9.
54. Liang HP, Tse ZTH. Cycloidal Stepper Motor: A Systematic Approach for Designing a Nonmagnetic Rotary Actuator. IEEE ASME Trans Mechatron. 2023;28(1):71-9.
55. Simonelli J, Lee YH, Chen CW, Li XZ, Mikaiel S, Lu D, Wu HH, Tsao TC. Hydrostatic actuation for remote operations in MR environment. IEEE ASME Trans Mechatron. 2020;25(2):894–905.
56. Pfeil A, Barbé L, Wach B, Bruyas A, Geiskopf F, Nierenberger M, Renaud P. A 3D-Printed Needle Driver Based on Auxetic Structure and Inchworm Kinematics. ASME International Design Engineering Technical Conferences and Computers and Information in Engineering Conference. 2018.
57. Fischer GS, Krieger A, Iordachita I, Csoma C, Whitcomb LL, Fichtinger G. MRI Compatibility of Robot Actuation Techniques – A Comparative Study. Medical Image Computing and Computer-Assisted Intervention (MICCAI). 2008.
58. Krieger A, Song SE, Cho NB, Iordachita II, Guion P, Fichtinger G, Whitcomb LL. Development and evaluation of an actuated MRI-compatible robotic system for MRI-guided prostate intervention. IEEE ASME Trans Mechatron. 2013;18(1):273–84.
59. Su H, Cole GA, Fischer GS. High-Field MRI-Compatible Needle Placement Robots for Prostate Interventions: Pneumatic and Piezoelectric Approaches. In: Gulrez T, Hassanien AE, editors. Advances in Robotics and Virtual Reality. Intelligent Systems Reference Library. Berlin, Heidelberg: Springer Berlin Heidelberg; 2012. p. 3–32.
60. Elbannan KM, Salisbury SP. Design of a two degree-of-freedom, MRI-compatible actuator. Annual International Conference of the IEEE Engineering in Medicine and Biology Society. 2012.
61. Vigaru B, Sulzer J, Gassert R. Design and evaluation of a cable-driven fMRI-compatible haptic interface to investigate precision grip control. IEEE Trans Haptics. 2016;9(1):20–32.
62. Airpot. https://www.airpot.com/.
63. Li M, Pal A, Aghakhani A, Pena-Francesch A, Sitti M. Soft actuators for real-world applications. Nat Rev Mater. 2022;7(3):235–49.
64. Gudino N, Heilman JA, Derakhshan JJ, Sunshine JL, Duerk JL, Griswold MA. Control of intravascular catheters using an array of active steering coils. Med Phys. 2011;38(7):4215–24.
65. Felfoul O, Becker A, Bergeles C, Dupont PE. Achieving commutation control of an mri-powered robot actuator. IEEE Trans Robot. 2015;31(2):387–99.
66. Kalmar M, Boese A, Maldonado I, Landes R, Friebe M. NITINOL-based actuator for device control even in high-field MRI environment. Med Devices Evid Res. 2019;12:285–96.
67. Jia X, Zhang Y, Jiang J, Du H, Yu Y. Design and analysis of a novel long-distance double tendon-sheath transmission device for breast intervention robots under MRI field. Adv Mech Eng. 2020;12(3):1687814020904565.
68. Monfaredi R, Seifabadi R, Fichtinger G, Iordachita I. Design of a decoupled MRI-compatible force sensor using fiber Bragg grating sensors for robot-assisted prostate interventions. Proc SPIE - Int Soc Opt Eng. 2013;8671:319–27.
69. Saccomandi P, Schena E, Giurazza F, Del Vescovo R, Caponero MA, Mortato L, Panzera F, Cazzato RL, Grasso FR, Di Matteo FM, Silvestri S, Zobel BB. Temperature monitoring and lesion volume estimation during double-applicator laser-induced thermotherapy in ex vivo swine pancreas: a preliminary study. Lasers Med Sci. 2014;29(2):607–14.
70. Taffoni F, Formica D, Saccomandi P, Di Pino G, Schena E. Optical fiber-based MR-compatible sensors for medical applications: an overview. Sensors. 2013;13(10):14105–20.
71. Jäckle S, Eixmann T, Schulz-Hildebrandt H, Hüttmann G, Pätz T. Fiber optical shape sensing of flexible instruments for endovascular navigation. Int J Comput Assist Radiol Surg. 2019;14(12):2137–45.
72. Huang S, Gao A, Wu Z, Lou C, Wang Y, Yang GZ. An MR safe rotary encoder based on eccentric sheave and FBG sensors. IEEE International Conference on Robotics and Automation (ICRA). 2021.
73. Polygerinos P, Seneviratne LD, Razavi R, Schaeffter T, Althoefer K. Triaxial catheter-tip force sensor for MRI-guided cardiac procedures. IEEE ASME Trans Mechatron. 2013;18(1):386–96.
74. Gassert R, Chapuis D, Bleuler H, Burdet E. Sensors for applications in magnetic resonance environments. IEEE ASME Trans Mechatron. 2008;13(3):335–44.
75. Micronor Sensors. https://micronor.com/.
76. Eggers H, Weiss S, Boernert P, Boesiger P. Image-based tracking of optically detunable parallel resonant circuits. Magn Reson Med. 2003;49(6):1163–74.
77. Alipour A, Gokyar S, Algin O, Atalar E, Demir HV. An inductively coupled ultra-thin, flexible, and passive RF resonator for

MRI marking and guiding purposes: Clinical feasibility. Magn Reson Med. 2018;80(1):361–70.
78. Stoianovici D, Jun C, Lim S, Li P, Petrisor D, Fricke S, Sharma K, Cleary K. Multi-imager compatible, MR safe, remote center of motion needle-guide robot. IEEE Trans Biomed Eng. 2018;65(1):165–77.
79. Nijsink H, Overduin CG, Brand P, De Jong SF, Borm PJA, Warlé MC, Fütterer JJ. Optimised passive marker device visibility and automatic marker detection for 3-T MRI-guided endovascular interventions: a pulsatile flow phantom study. Eur Radiol Exp. 2022;6(1):11.
80. Elayaperumal S, Bae JH, Daniel BL, Cutkosky MR. Detection of membrane puncture with haptic feedback using a tip-force sensing needle. IEEE/RSJ International Conference on Intelligent Robots and Systems (IROS). 2014.
81. Beekley Corp. https://beekley.com/mri/mr-spot-skin-markers.
82. Su H, Iordachita II, Tokuda J, Hata N, Liu X, Seifabadi R, Xu S, Wood B, Fischer GS. Fiber optic force sensors for MRI-guided interventions and rehabilitation: a review. IEEE Sens J. 2017;17(7):1952–63.
83. Gu H, Fu Z, Fu Z, Lu C, Fei J, Guan Y. binocular vision-guided puncture needle automatic positioning method. 7th International Conference on Cloud Computing and Big Data Analytics (ICCCBDA). 2022.
84. Mao X, Xu J, Cui H. Functional nanoparticles for magnetic resonance imaging. Wiley Interdiscip Rev Nanomed Nanobiotechnol. 2016;8(6):814–41.
85. Gilad AA, Ziv K, McMahon MT, Van Zijl PC, Neeman M, Bulte JW. MRI reporter genes. J Nucl Med. 2008;49(12):1905–8.
86. Lundqvist M, Levin L. Cost-effectiveness of the use of Gold Anchor™ markers in prostate cancer. Cureus. 2020;12(10): e11229.
87. Wang T, Ciobanu L, Zhang X, Webb A. Inductively coupled RF coil design for simultaneous microimaging of multiple samples. Concepts Magn Reson Part B Magn Reson Eng. 2008;33(4):236–43.
88. Holton A, Walsh E, Anayiotos A, Pohost G, Venugopalan R. Comparative MRI compatibility of 316 L stainless steel alloy and nickel-titanium alloy stents. J Cardiovasc Magn Reson. 2002;4(4):423–30.
89. Ihira R, Gwon H, Kasada R, Konishi S. Improvement of tensile properties of pure Cu and CuCrZr alloy by cryo-rolling process. Fusion Eng Des. 2016;109–111:485–8.
90. Fonda P, Wang Z, Yamazaki K, Akutsu Y. A fundamental study on Ti–6Al–4V's thermal and electrical properties and their relation to EDM productivity. J Mater Process Technol. 2008;202(1):583–9.
91. Calin M, Vishnu J, Thirathipviwat P, Popa M-M, Krautz M, Manivasagam G, Gebert A. Tailoring biocompatible Ti-Zr-Nb-Hf-Si metallic glasses based on high-entropy alloys design approach. Mater Sci Eng C. 2021;121: 111733.
92. Schroers J, Lohwongwatana B, Johnson WL, Peker A. Gold based bulk metallic glass. 2005;87(6): 061912.
93. Pang S, Liu Y, Li H, Sun L, Li Y, Zhang T. New Ti-based Ti–Cu–Zr–Fe–Sn–Si–Ag bulk metallic glass for biomedical applications. J Alloys Compd. 2015;625:323–7.
94. Wapler MC, Leupold J, Dragonu I, von Elverfeld D, Zaitsev M, Wallrabe U. Magnetic properties of materials for MR engineering, micro-MR and beyond. J Magn Reson Imaging. 2014;242:233–42.
95. Mirdehghan SA. 1 - Fibrous polymeric composites. In: Latifi M, editor. Engineered Polymeric Fibrous Materials: Woodhead Publishing; 2021. p. 1–58.
96. Kwon OH, Jang C, Lee J, Jeong HY, Kwon YI, Joo JH, Kim H. Investigation of the electrical conductivity of sintered monoclinic zirconia (ZrO2). Ceram Int. 2017;43(11):8236–45.
97. Nakai R, Goto K, Shima K, Kodama T, Iwata H. Dual-phase Au-Pt alloys free from magnetic susceptibility artifacts in magnetic resonance imaging. Magn Reson Imaging. 2022;85:19–27.
98. Yang Y, Castany P, Cornen M, Prima F, Li SJ, Hao YL, Gloriant T. Characterization of the martensitic transformation in the superelastic Ti–24Nb–4Zr–8Sn alloy by in situ synchrotron X-ray diffraction and dynamic mechanical analysis. Acta Mater. 2015;88:25–33.
99. Nomura N, Tanaka Y, Suyalatu, Kondo R, Doi H, Tsutsumi Y, Hanawa T. Effects of Phase Constitution of Zr-Nb Alloys on Their Magnetic Susceptibilities. Mater Trans. 2009;50(10):2466–72.
100. Lv JW, Wei C, Zhang S, Shi ZL, Zhang HR, Zhang XY, Ma MZ. Microstructure and mechanical behavior evolution of Ti-based bulk metallic glass induced by sub-Tg isothermal annealing. J Alloys Compd. 2022;900: 163300.
101. Ebnesajjad S. 5 - Expansion of Polytetrafluoroethylene Resins. In: Ebnesajjad S, editor. Expanded PTFE Applications Handbook. Oxford: William Andrew Publishing; 2017. p. 99–127.
102. Rinaldi M, Cecchini F, Pigliaru L, Ghidini T, Lumaca F, Nanni F. Additive manufacturing of polyether ether ketone (PEEK) for space applications: a nanosat polymeric structure. Polymers. 2021;13(1):11.
103. Tekinalp HL, Kunc V, Velez-Garcia GM, Duty CE, Love LJ, Naskar AK, Blue CA, Ozcan S. Highly oriented carbon fiber–polymer composites via additive manufacturing. Compos Sci Technol. 2014;105:144–50.
104. Huang X, Zhou Y, Wang C, Qi F, Luo P, Du H, Zhang Q, Liu Z, Yuan K, Qiu B. Development of a novel MR-conditional microwave needle for MR-guided interventional microwave ablation at 1.5T. Magn Reson Med. 2022;88(4):1886–900.
105. Li S, Xie Z, Xue W. Microstructure and mechanical properties of zirconia ceramics consolidated by a novel oscillatory pressure sintering. Ceram Int. 2015;41(8):10281–6.
106. Murbach M, Zastrow E, Neufeld E, Cabot E, Kainz W, Kuster N. Heating and safety concerns of the radio-frequency field in MRI. Curr Radiol Rep. 2015;3(12):45.
107. Li H-Z, Xu J. MRI compatible Nb–Ta–Zr alloys used for vascular stents: optimization for mechanical properties. J Mech Behav Biomed Mater. 2014;32:166–76.
108. Kondo R, Nomura, Suyalatu N, Tsutsumi Y, Doi H, Hanawa T. Microstructure and mechanical properties of as-cast Zr–Nb alloys. Acta Biomater. 2011;7(12):4278–84.
109. Suyalatu, Kondo R, Tsutsumi Y, Doi H, Nomura N, Hanawa T. Effects of phase constitution on magnetic susceptibility and mechanical properties of Zr-rich Zr–Mo alloys. Acta Biomater. 2011;7(12):4259–66.
110. Suyalatu, Nomura N, Oya K, Tanaka Y, Kondo R, Doi H, Tsutsumi Y, Hanawa T. Microstructure and magnetic susceptibility of as-cast Zr–Mo alloys. Acta Biomater. 2010;6(3):1033–8.
111. Astary GW, Peprah MK, Fisher CR, Stewart RL, Carney PR, Sarntinoranont M, Meisel MW, Manuel MV, Mareci TH. MR measurement of alloy magnetic susceptibility: Towards developing tissue-susceptibility matched metals. J Magn Reson. 2013;233:49–55.
112. Brunette DM, Tengvall P, Textor M, Thomsen P. Titanium in medicine: material science, surface science, engineering, biological responses and medical applications: Springer; 2001.
113. Ijaz MF, Kim HY, Hosoda H, Miyazaki S. Superelastic properties of biomedical (Ti–Zr)–Mo–Sn alloys. Mater Sci Eng C. 2015;48:11–20.
114. López Pavón L, Kim HY, Hosoda H, Miyazaki S. Effect of Nb content and heat treatment temperature on superelastic properties of Ti–24Zr–(8–12)Nb–2Sn alloys. Scr Mater. 2015;95:46–9.

115. Park JM, Wang G, Pauly S, Mattern N, Kim DH, Eckert J. Ductile ti-based bulk metallic glasses with high specific strength. Metall Mater Trans A. 2011;42(6):1456–62.
116. Zhou FY, Qiu KJ, Li HF, Huang T, Wang BL, Li L, Zheng YF. Screening on binary Zr–1X (X=Ti, Nb, Mo, Cu, Au, Pd, Ag, Ru, Hf and Bi) alloys with good in vitro cytocompatibility and magnetic resonance imaging compatibility. Acta Biomater. 2013;9(12):9578–87.
117. Kodama T, Nakai R, Goto K, Shima K, Iwata H. Preparation of an Au-Pt alloy free from artifacts in magnetic resonance imaging. Magn Reson Imaging. 2017;44:38–45.
118. Hempel E, Fischer H, Gumb L, Höhn T, Krause H, Voges U, Breitwieser H, Gutmann B, Durke J, Bock M, Melzer A. An MRI-compatible surgical robot for precise radiological interventions. Comput Aided Surg. 2003;8(4):180–91.
119. Muntener M, Patriciu A, Petrisor D, Mazilu D, Bagga H, Kavoussi L, Cleary K, Stoianovici D. Magnetic resonance imaging compatible robotic system for fully automated brachytherapy seed placement. Surg Today. 2006;68(6):1313–7.
120. Cleary K, Melzer A, Watson V, Kronreif G, Stoianovici D. Interventional robotic systems: applications and technology state-of-the-art. Minim Invasive Ther Allied Technol. 2006;15(2):101–13.
121. Zhang YW, Li SJ, Obbard EG, Wang H, Wang SC, Hao YL, Yang R. Elastic properties of Ti–24Nb–4Zr–8Sn single crystals with bcc crystal structure. Acta Mater. 2011;59(8):3081–90.
122. Yamato M, Aoki H, Kimura T, Yamamoto I, Ishikawa F, Yamaguchi M, Tobita M. Determination of anisotropic diamagnetic susceptibility of polymeric fibers suspended in liquid. Jpn J Appl Phys. 2001;40(4R):2237.
123. Neumann W, Pusch TP, Siegfarth M, Schad LR, Stallkamp JL. CT and MRI compatibility of flexible 3D-printed materials for soft actuators and robots used in image-guided interventions. Med Phys. 2019;46(12):5488–98.
124. Moses ZB, Lee TC, Huang KT, Guenette JP, Chi JH. MRI-guided cryoablation for metastatic spine disease: intermediate-term clinical outcomes in 14 consecutive patients. J Neurosurg Spine. 2020;32(5):676–81.
125. Overduin CG, Jenniskens SFM, Sedelaar JPM, Bomers JGR, Fütterer JJ. Percutaneous MR-guided focal cryoablation for recurrent prostate cancer following radiation therapy: retrospective analysis of iceball margins and outcomes. Eur Radiol. 2017;27(11):4828–36.
126. MacDonell J, Patel N, Fischer G, Burdette EC, Qian J, Chumbalkar V, Ghoshal G, Heffter T, Williams E, Gounis M, King R, Thibodeau J, Bogdanov G, Brooks OW, Langan E, Hwang R, Pilitsis JG. Robotic assisted MRI-guided interventional interstitial MR-guided focused ultrasound ablation in a swine model. Neurosurg. 2019;84(5):1138–48.
127. Han SJ, Bankiewicz K, Butowski NA, Larson PS, Aghi MK. Interventional MRI-guided catheter placement and real time drug delivery to the central nervous system. Expert Rev Neurother. 2016;16(6):635–9.
128. Zhao S, Li G, Tong C, Chen W, Wang P, Dai J, Fu X, Xu Z, Liu X, Lu L, Liang Z, Duan X. Full activation pattern mapping by simultaneous deep brain stimulation and fMRI with graphene fiber electrodes. Nat Commun. 2020;11(1):1788.
129. Woodrum DA, Gorny KR, Greenwood B, Mynderse LA. MRI-Guided Prostate Biopsy of Native and Recurrent Prostate Cancer. Semin intervent Radiol. 2016;33(03):196–205.
130. Kilbride BF, Jordan CD, Chu A, Barry D, Mueller K, Ahn S, Moore T, Wilson MW, Hetts SW. Development and Evaluation of an MR-safe Interventional Catheter with Tunable MR Visibility and Radiopacity. ISMRM & SMRT Annual Meeting. 2021.
131. Veeram Reddy SR, Arar Y, Zahr RA, Gooty V, Hernandez J, Potersnak A, Douglas P, Blair Z, Greer JS, Roujol S, Forte MNV, Greil G, Nugent AW, Hussain T. Invasive cardiovascular magnetic resonance (iCMR) for diagnostic right and left heart catheterization using an MR-conditional guidewire and passive visualization in congenital heart disease. J Cardiovasc Magn Reson. 2020;22(1):20.
132. Schmidt EJ, Morcos M, Gunderman A, Tokuda J, Seethamraju RT, Neri L, Kut C, Halperin HR, Viswanathan AN, Chen Y. An MR-Tracked Metallic injection needle for Distancing Radiation-sources from Sensitive tissues: Construct and Initial testing in Swine. ISMRM & SMRT Annual Meeting. 2021.
133. Vitzthum HE, Winkler D, Strauss G, Lindner D, Krupp W, Schneider JP, Schober R, Meixensberger J. NEUROGATE®: A new MR-compatible device for realizing minimally invasive treatment of intracerebral tumors. Comput Aided Surg. 2004;9(1–2):45–50.
134. Carpentier A, Chauvet D, Reina V, Beccaria K, Leclerq D, McNichols RJ, Gowda A, Cornu P, Delattre J-Y. MR-guided laser-induced thermal therapy (LITT) for recurrent glioblastomas. Lasers Surg Med. 2012;44(5):361–8.
135. Jameel A, Bain P, Nandi D, Jones B, Gedroyc W. Device profile of exAblate Neuro 4000, the leading system for brain magnetic resonance guided focused ultrasound technology: an overview of its safety and efficacy in the treatment of medically refractory essential tremor. Expert Rev Med Devices. 2021;18(5):429–37.
136. MacDonell J, Patel N, Rubino S, Ghoshal G, Fischer G, Burdette EC, Hwang R, Pilitsis JG. Magnetic resonance–guided interstitial high-intensity focused ultrasound for brain tumor ablation. Neurosurg Focus. 2018;44(2):E11.
137. Kholmovski EG, Coulombe N, Silvernagel J, Angel N, Parker D, Macleod R, Marrouche N, Ranjan R. Real-time MRI-guided cardiac cryo-ablation: a feasibility study. J Cardiovasc Electrophysiol. 2016;27(5):602–8.
138. Winkelmann MT, Gohla G, Kübler J, Weiß J, Clasen S, Nikolaou K, Hoffmann R. MR-guided high-power microwave ablation in hepatic malignancies: initial results in clinical routine. Cardiovasc Intervent Radiol. 2020;43(11):1631–8.
139. Murakami K, Naka S, Shiomi H, Akabori H, Kurumi Y, Morikawa S, Tani T. Initial experiences with MR Image-guided laparoscopic microwave coagulation therapy for hepatic tumors. Surg Today. 2015;45(9):1173–8.
140. Medtronic Percept PC. https://www.medtronic.com/us-en/patients/treatments-therapies/deep-brain-stimulation-parkinsons-disease/about-dbs-therapy/dbs-products/percept-pc.html.
141. Larson PS, Starr PA, Martin AJ. Deep brain stimulation: interventional and intraoperative MRI approaches. Curr Concepts Mov Disord Mgmt. 2018;33:187–97.
142. Richards HK, Seeley HM, Pickard JD. Efficacy of antibiotic-impregnated shunt catheters in reducing shunt infection: data from the United Kingdom Shunt Registry. Clinical article J Neurosurg Pediatr. 2009;4(4):389–93.
143. Lang ML, Zhang Q, Chen X, Yan N, Zhu H, Martin M, Yu F, Niu C, Zhang G, Zeng Q. First ground-based, high-field, cryogen-free, mobile intraoperative magnetic resonance imaging system. Magn Reson Imaging. 2023;99:34–40.
144. Beyersdorff D, Winkel A, Hamm B, Lenk S, Loening SA, Taupitz M. MR imaging–guided prostate biopsy with a closed MR unit at 1.5 T: initial results. Radiology. 2005;234(2):576–81.
145. Ghiatas Beaded Breast Localization Wire. https://www.bd.com/en-us/products-and-solutions/products/product-families/ghiatas-beaded-breast-localization-wire.
146. Heidt T, Reiss S, Krafft AJ, Özen AC, Lottner T, Hehrlein C, Galmbacher R, Kayser G, Hilgendorf I, Stachon P, Wolf D, Zirlik A, Düring K, Zehender M, Meckel S, von Elverfeldt D, Bode C, Bock M, von zur Mühlen C. Real-time magnetic resonance imaging – guided coronary intervention in a porcine model. Sci Rep. 2019;9(1):8663.

147. Knight DS, Kotecha T, Martinez-Naharro A, Brown JT, Bertelli M, Fontana M, Muthurangu V, Coghlan JG. Cardiovascular magnetic resonance-guided right heart catheterization in a conventional CMR environment – predictors of procedure success and duration in pulmonary artery hypertension. J Cardiovasc Magn Reson. 2019;21(1):57.
148. Streitparth F, De Bucourt M, Hartwig T, Leidenberger T, Rump J, Walter T, Maurer M, Renz D, Stelter L, Wiener E, Hamm B, Teichgräber U. Real-time MR-guided lumbosacral periradicular injection therapy using an open 1.0-t mri system: an outcome study. Invest Radiol. 2013;48(6):471–6.
149. Chen C, Lee I, Tatsui C, Elder T, Sloan AE. Laser interstitial thermotherapy (LITT) for the treatment of tumors of the brain and spine: a brief review. J Neuro-Oncol. 2021;151(3):429–42.
150. Hawasli AH, Bagade S, Shimony JS, Miller-Thomas M, Leuthardt EC. Magnetic resonance imaging-guided focused laser interstitial thermal therapy for intracranial lesions: Single-institution series. Neurosurg. 2013;73(6):1007–17.
151. Karampelas I, Sloan AE. Laser-induced interstitial thermotherapy of gliomas. Prog neurol surg. 2018;32:14–26.
152. Hynynen K. MRI-guided focused ultrasound treatments. Ultrasonics. 2010;50(2):221–9.
153. Sayed D, Chakravarthy K, Amirdelfan K, Kalia H, Meacham K, Shirvalkar P, Falowski S, Petersen E, Hagedorn JM, Pope J, Leever J, Deer T. A comprehensive practice guideline for magnetic resonance imaging compatibility in implanted neuromodulation devices. Neuromodulation. 2020;23(7):893–911 Technology at the Neural Interface.
154. Miocinovic S, Somayajula S, Chitnis S, Vitek JL. History, applications, and mechanisms of deep brain stimulation. JAMA Neurol. 2013;70(2):163–71.
155. Ostrem JL, Ziman N, Galifianakis NB, Starr PA, Luciano MS, Katz M, Racine CA, Martin AJ, Markun LC, Larson PS. Clinical outcomes using ClearPoint interventional MRI for deep brain stimulation lead placement in Parkinson's disease. J Neurosurg. 2016;124(4):908–16.
156. Lee AT, Han KJ, Nichols N, Sudhakar VR, Burke JF, Wozny TA, Chung JE, Volz MM, Ostrem JL, Martin AJ, Larson PS, Starr PA, Wang DD. Targeting accuracy and clinical outcomes of awake versus asleep interventional magnetic resonance imaging-guided deep brain stimulation for Parkinson's disease: The University of California. San Francisco Experience Neurosurg. 2022;91(5):717–25.
157. Boutet A, Rashid T, Hancu I, Elias GJB, Gramer RM, Germann J, Dimarzio M, Li B, Paramanandam V, Prasad S, Ranjan M, Coblentz A, Gwun D, Chow CT, Maciel R, Soh D, Fiveland E, Hodaie M, Kalia SK, Fasano A, Kucharczyk W, Pilitsis J, Lozano AM. Functional MRI safety and artifacts during deep brain stimulation: experience in 102 patients. Radiology. 2019;293(1):174–83.
158. Kapoor MM, Patel MM, Scoggins ME. The wire and beyond: recent advances in breast imaging preoperative needle localization. Radiographics. 2019;39(7):1886–906.
159. Panebianco V, Barchetti F, Manenti G, Aversa T, Catalano C, Simonetti G. MR imaging-guided prostate biopsy: technical features and preliminary results. Radiol Med. 2015;120(6):571–8.
160. Verma S, Choyke PL, Eberhardt SC, Oto A, Tempany CM, Turkbey B, Rosenkrantz AB. The Current State of MR imaging–targeted biopsy techniques for detection of prostate cancer. Radiology. 2017;285(2):343–56.
161. Williams J. Evaluating EPflex MRline guidewire for endovascular interventions guided by MRI at 3T vs. X-ray fluoroscopy. San Francisco: University of California; 2019.
162. Clogenson HCM. MRI-Compatible Endovascular Instruments 2014.
163. Reimer P, Meaney JFM, Parizel PM, Stichnoth FA. Clinical MR Imaging (Third Edition): A Practical Approach: Springer; 2010. 1–820 p.
164. Li Y, Wang T, Zhang T, Lin Z, Li Y, Guo R, Zhao Y, Meng Z, Liu J, Yu X, Liang ZP, Nachev P. Fast high-resolution metabolic imaging of acute stroke with 3D magnetic resonance spectroscopy. Brain. 2020;143(11):3225–33.
165. SIEMENS Healthineers. https://www.siemens-healthineers.com/magnetic-resonance-imaging/0-35-to-1-5t-mri-scanner/magnetom-sola.
166. SIEMENS Healthineers. https://www.siemens-healthineers.com/magnetic-resonance-imaging/3t-mri-scanner/magnetom-vida.
167. Cheng SS, Wang X, Jeong S, Kole M, Roys S, Gullapalli RP. Mechanical Design and Evaluation of a Selectively-actuated MRI-compatible Continuum Neurosurgical Robot. IEEE/RSJ International Conference on Intelligent Robots and Systems (IROS). 2021.
168. Li G, Patel NA, Wang Y, Dumoulin C, Loew W, Loparo O, Schneider K, Sharma K, Cleary K, Fritz J, Iordachita I. Fully actuated body-mounted robotic system for MRI-guided lower back pain injections: initial phantom and cadaver studies. IEEE Robot Autom Lett. 2020;5(4):5245–51.
169. Mikaiel S, Simonelli J, Li X, Lee YH, Lee YS, Sung K, Lu DS, Tsao TC, Wu HH. MRI-guided targeted needle placement during motion using hydrostatic actuators. Int J Med Robot. 2020;16(2): e2041.
170. Su H, Zervas M, Cole GA, Furlong C, Fischer GS, Ieee. Real-time MRI-Guided Needle Placement Robot with Integrated Fiber Optic Force Sensing. IEEE International Conference on Robotics and Automation (ICRA). 2011. Shanghai, China.
171. Yakar D, Schouten MG, Bosboom DGH, Barentsz JO, Scheenen TWJ, Fuetterer JJ. Feasibility of a pneumatically actuated MR-compatible robot for transrectal prostate biopsy guidance. Radiology. 2011;260(1):241–7.
172. Giannakou M, Drakos T, Menikou G, Evripidou N, Filippou A, Spanoudes K, Ioannou L, Damianou C. Magnetic resonance image-guided focused ultrasound robotic system for transrectal prostate cancer therapy. Int J Med Robot. 2021;17(3): e2237.
173. Patel NA, Nycz CJ, Carvalho PA, Gandomi KY, Gondokaryono R, Li G, Heffter T, Burdette EC, Pilitsis JG, Fischer GS. An integrated robotic system for mri-guided neuroablation: preclinical evaluation. IEEE Trans Biomed Eng. 2020;67(10):2990–9.
174. Monteris Medical. https://www.monteris.com/.
175. neuroArm. https://neuroarm.org/.
176. Eslami S, Shang W, Li G, Patel N, Fischer GS, Tokuda J, Hata N, Tempany CM, Iordachita I. In-bore prostate transperineal interventions with an MRI-guided parallel manipulator: system development and preliminary evaluation. Int J Med Robot Comput Assist Surg. 2016;12(2):199–213.
177. MrBot. https://urobotics.urology.jhu.edu/.
178. Soteria Medical. https://www.soteria-medical.com/.
179. Lam F, Liang ZP. A subspace approach to high-resolution spectroscopic imaging. Magn Reson Med. 2014;71(4):1349–57.
180. Nayak KS, Lim Y, Campbell-Washburn AE, Steeden J. Real-time magnetic resonance imaging. J Magn Reson Imaging. 2020;55(1):81–99.
181. Schulder M, Miller JP. Robotic asisted MRI-guided interventional interstitial MR-guided focused ultrasound ablation in a swine model COMMENT. Neurosurgery. 2019;84(5):1147–8.
182. Tokuda J, Song SE, Tuncali K, Tempany C, Hata N. Configurable automatic detection and registration of fiducial frames for device-to-image registration in MRI-guided prostate interventions. Lect Notes Comput Sc. 2013;8151:355–62.
183. Krieger A, Iordachita II, Guion P, Singh AK, Kaushal A, Menard C, Pinto PA, Camphausen K, Fichtinger G, Whitcomb LL. An MRI-compatible robotic system with hybrid tracking

for MRI-guided prostate intervention. IEEE Trans Biomed Eng. 2011;58(11):3049–60.
184. Fedorov A, Beichel R, Kalpathy-Cramer J, Finet J, Fillion-Robin JC, Pujol S, Bauer C, Jennings D, Fennessy F, Sonka M, Buatti J, Aylward S, Miller JV, Pieper S, Kikinis R. 3D Slicer as an image computing platform for the quantitative Imaging Network. Magn Reson Imaging. 2012;30(9):1323–41.
185. Mansfield P. Multi-planar image-formation using nmr spin echoes. J Phys C Solid State. 1977;10(3):L55–8.
186. Shankaranarayanan A, Wendt M, Aschoff AJ, Lewin JS, Duerk JL. Radial keyhole sequences for low field projection reconstruction interventional MRI. J Magn Reson Imaging. 2001;13(1):142–51.
187. Jaubert O, Montalt-Tordera J, Knight D, Coghlan GJ, Arridge S, Steeden JA, Muthurangu V. Real-time deep artifact suppression using recurrent U-Nets for low-latency cardiac MRI. Magn Reson Med. 2021;86(4):1904–16.
188. Kleineisel J, Heidenreich JF, Eirich P, Petri N, Kostler H, Petritsch B, Bley TA, Wech T. Real-time cardiac MRI using an undersampled spiral k-space trajectory and a reconstruction based on a variational network. Magn Reson Med. 2022;88(5):2167–78.
189. Feng L. Golden-angle radial MRI: basics, advances, and applications. J Magn Reson Imaging. 2022;56(1):45–62.
190. Feng L, Coppo S, Piccini D, Yerly J, Lim RP, Masci PG, Stuber M, Sodickson DK, Otazo R. 5D whole-heart sparse MRI. Magn Reson Med. 2018;79(2):826–38.
191. Campbell-Washburn AE, Faranesh AZ, Lederman RJ, Hansen MS. Magnetic resonance sequences and rapid acquisition for MR-guided interventions. Magn Reson Imaging Clin N Am. 2015;23(4):669–79.
192. Pruessmann KP, Weiger M, Scheidegger MB, Boesiger P. SENSE: sensitivity encoding for fast MRI. Magn Reson Med. 2015;42(5):952–62.
193. Griswold MA, Jakob PM, Heidemann RM, Nittka M, Jellus V, Wang J, Kiefer B, Haase A. Generalized autocalibrating partially parallel acquisitions (GRAPPA). Magn Reson Med. 2002;47(6):1202–10.
194. Lustig M, Pauly JM. SPIRiT: Iterative self-consistent parallel imaging reconstruction from arbitrary k-space. Magn Reson Med. 2010;64(2):457–71.
195. Uecker M, Lai P, Murphy MJ, Virtue P, Elad M, Pauly JM, Vasanawala SS, Lustig M. ESPIRiT–an eigenvalue approach to autocalibrating parallel MRI: where SENSE meets GRAPPA. Magn Reson Med. 2014;71(3):990–1001.
196. Hamilton J, Franson D, Seiberlich N. Recent advances in parallel imaging for MRI. Prog Nucl Magn Reson Spectrosc. 2017;101:71–95.
197. Doneva M, Bornert P. Automatic coil selection for channel reduction in SENSE-based parallel imaging. Magn Reson Mater Phy Biol Med. 2008;21(3):187–96.
198. Buehrer M, Pruessmann KP, Boesiger P, Kozerke S. Array compression for MRI with large coil arrays. Magn Reson Med. 2007;57(6):1131–9.
199. Haacke EM, Liang ZP, Izen SH. Constrained reconstruction: a superresolution, optimal signal-to-noise alternative to the Fourier transform in magnetic resonance imaging. Med Phys. 1989;16(3):388–97.
200. Liang ZP, Lauterbur PC. An efficient method for dynamic magnetic resonance imaging. IEEE Trans Med Imaging. 1994;13(4):677–86.
201. Liang ZP, Lauterbur PC. A generalized series approach to MR spectroscopic imaging. IEEE Trans Med Imaging. 1991;10(2):132–7.
202. Madore B, Glover GH, Pelc NJ. Unaliasing by Fourier-encoding the overlaps using the temporal dimension (UNFOLD), applied to cardiac imaging and fMRI. Magn Reson Med. 1999;42(5):813–28.
203. Tsao J, Boesiger P, Pruessmann KP. k-t BLAST and k-t SENSE: Dynamic MRI with high frame rate exploiting spatiotemporal correlations. Magn Reson Med. 2003;50(5):1031–42.
204. Lustig M, Donoho D, Pauly JM. Sparse MRI: The application of compressed sensing for rapid MR imaging. Magn Reson Med. 2007;58(6):1182–95.
205. Sandino CM, Cheng JY, Chen F, Mardani M, Pauly JM, Vasanawala SS. Compressed sensing: from research to clinical practice with deep neural networks. IEEE Signal Process Mag. 2020;37(1):111–27.
206. Jung H, Sung K, Nayak KS, Kim EY, Ye JC. k-t FOCUSS: a general compressed sensing framework for high resolution dynamic MRI. Magn Reson Med. 2009;61(1):103–16.
207. Feng L, Grimm R, Block KT, Chandarana H, Kim S, Xu J, Axel L, Sodickson DK, Otazo R. Golden-angle radial sparse parallel MRI: combination of compressed sensing, parallel imaging, and golden-angle radial sampling for fast and flexible dynamic volumetric MRI. Magn Reson Med. 2014;72(3):707–17.
208. Liang ZP. Spatiotemporal Imaging with partially separable functions. Joint Meeting of the 6th International Symposium on Noninvasive Functional Source Imaging of the Brain and Heart and the International Conference on Functional Biomedical Imaging. 2007.
209. He JF, Liu QG, Christodoulou AG, Ma C, Lam F, Liang ZP. Accelerated high-dimensional MR imaging with sparse sampling using low-rank tensors. IEEE Trans Med Imaging. 2016;35(9):2119–29.
210. Zhao B, Haldar JP, Christodoulou AG, Liang ZP. Image reconstruction from highly undersampled (k, t)-space data with joint partial separability and sparsity constraints. IEEE Trans Med Imaging. 2012;31(9):1809–20.
211. Lingala SG, Hu Y, Dibella E, Jacob M. Accelerated dynamic MRI exploiting sparsity and low-rank structure: k-t SLR. IEEE Trans Med Imaging. 2011;30(5):1042–54.
212. Tremoulheac B, Dikaios N, Atkinson D, Arridge SR. Dynamic MR image reconstruction–separation from undersampled (k, t)-space via low-rank plus sparse prior. IEEE Trans Med Imaging. 2014;33(8):1689–701.
213. Otazo R, Candes E, Sodickson DK. Low-rank plus sparse matrix decomposition for accelerated dynamic MRI with separation of background and dynamic components. Magn Reson Med. 2015;73(3):1125–36.
214. Cao Z, Gore JC, Grissom WA. Low-rank plus sparse compressed sensing for accelerated proton resonance frequency shift MR temperature imaging. Magn Reson Med. 2019;81(6):3555–66.
215. He Z, Zhu Y-N, Qiu S, Wang T, Zhang C, Sun B, Zhang X, Feng Y. Low-rank and framelet based sparsity decomposition for interventional MRI reconstruction. IEEE Trans Biomed Eng. 2022;69(7):2294–304.
216. Unterberg-Buchwald C, Ritter CO, Reupke V, Wilke RN, Stadelmann C, Steinmetz M, Schuster A, Hasenfuss G, Lotz J, Uecker M. Targeted endomyocardial biopsy guided by real-time cardiovascular magnetic resonance. J Cardiovasc Magn Reson. 2017;19(1):45.
217. Wang S, Su Z, Ying L, Xi P, Dong L. Accelerating magnetic resonance imaging via deep learning. IEEE International Symposium on Biomedical Imaging. 2016.
218. Wang G, Ye JC, De Man B. Deep learning for tomographic image reconstruction. Nat Mach Intell. 2020;2(12):737–48.
219. Chen Y, Schonlieb C-B, Lio P, Leiner T, Dragotti PL, Wang G, Rueckert D, Firmin D, Yang G. AI-based reconstruction for fast MRI—a systematic review and meta-analysis. Proc IEEE. 2022;110(2):224–45.
220. Wang S, Xiao T, Liu Q, Zheng H. Deep learning for fast MR imaging: a review for learning reconstruction from incomplete k-space data. Biomed Signal Process Control. 2021;68:102579.

221. Liang D, Cheng J, Ke Z, Ying L. Deep magnetic resonance image reconstruction: inverse problems meet neural networks. IEEE Signal Process Mag. 2020;37(1):141–51.
222. Zhu B, Liu JZ, Cauley SF, Rosen BR, Rosen MS. Image reconstruction by domain-transform manifold learning. Nature. 2018;555(7697):487–92.
223. Oh C, Kim D, Chung JY, Han Y, Park H. ETER-net: End to End MR image reconstruction using recurrent neural network. machine learning for medical image reconstruction. 2018.
224. Yang G, Yu S, Dong H, Slabaugh G, Dragotti PL, Ye X, Liu F, Arridge S, Keegan J, Guo Y, Firmin D, Keegan J, Slabaugh G, Arridge S, Ye X, Guo Y, Yu S, Liu F, Firmin D, Dragotti PL, Yang G, Dong H. DAGAN: deep de-aliasing generative adversarial networks for fast compressed sensing MRI reconstruction. IEEE Trans Med Imaging. 2018;37(6):1310–21.
225. Schlemper J, Caballero J, Hajnal JV, Price AN, Rueckert D. A Deep Cascade of Convolutional Neural Networks for Dynamic MR Image Reconstruction. IEEE Trans Med Imaging. 2018;37(2):491–503.
226. Yang Y, Sun J, Li H, Xu Z. ADMM-CSNet: a deep learning approach for image compressive sensing. IEEE Trans Pattern Anal Mach Intell. 2020;42(3):521–38.
227. Zhang J, Ghanem B. ISTA-Net: Interpretable Optimization-Inspired Deep Network for Image Compressive Sensing. IEEE/CVF Conference on Computer Vision and Pattern Recognition (CVPR). 2018.
228. Ke Z, Huang W, Cui ZX, Cheng J, Jia S, Wang H, Liu X, Zheng H, Ying L, Zhu Y, Liang D. Learned Low-rank Priors in Dynamic MR Imaging. IEEE Trans Med Imaging. 2021.
229. Huang W, Ke Z, Cui ZX, Cheng J, Qiu Z, Jia S, Ying L, Zhu Y, Liang D. Deep low-rank plus sparse network for dynamic MR imaging. Med Image Anal. 2021;73: 102190.
230. Zufiria B, Qiu S, Yan K, Zhao R, Wang R, She H, Zhang C, Sun B, Herman P, Du Y, Feng Y. A feature-based convolutional neural network for reconstruction of interventional MRI. NMR Biomed. 2019:e4231.
231. Terpstra ML, Maspero M, d'Agata F, Stemkens B, Intven MPW, Lagendijk JJW, van den Berg CAT, Tijssen RHN. Deep learning-based image reconstruction and motion estimation from undersampled radial k-space for real-time MRI-guided radiotherapy. Phys Med Biol. 2020;65(15): 155015.
232. Zhou B, Schlemper J, Dey N, Mohseni Salehi SS, Sheth K, Liu C, Duncan JS, Sofka M. Dual-domain self-supervised learning for accelerated non-Cartesian MRI reconstruction. Med Image Anal. 2022;81: 102538.
233. Korkmaz Y, Dar SU, Yurt M, Ozbey M, Cukur T. Unsupervised MRI Reconstruction via zero-shot learned adversarial transformers. IEEE Trans Med Imaging. 2022;41(7):1747–63.
234. Feng CM, Yan Y, Chen G, Xu Y, Hu Y, Shao L, Fu H. Multi-Modal Transformer for Accelerated MR Imaging. IEEE Trans Med Imaging. 2022:1.
235. Chung H, Ye JC. Score-based diffusion models for accelerated MRI. Med Image Anal. 2022;80: 102479.
236. Stone SS, Haldar JP, Tsao SC, Hwu WMW, Sutton BP, Liang ZP. Accelerating advanced MRI reconstructions on GPUs. J Parallel Distr Com. 2008;68(10):1307–18.
237. Schaetz S, Voit D, Frahm J, Uecker M. Accelerated computing in magnetic resonance imaging: real-time imaging using nonlinear inverse reconstruction. Comput Math Methods Med. 2017;2017:3527269.
238. Akkus Z, Galimzianova A, Hoogi A, Rubin DL, Erickson BJ. Deep learning for brain MRI segmentation: state of the art and future directions. J Digit Imaging. 2017;30(4):449–59.
239. Virzi A, Muller CO, Marret JB, Mille E, Berteloot L, Grevent D, Boddaert N, Gori P, Sarnacki S, Bloch I. Comprehensive review of 3D segmentation software tools for MRI usable for pelvic surgery planning. J Digit Imaging. 2020;33(1):99–110.
240. Tavakkolmoghaddam F, Rajamani DK, Szewczyk B, Zhao Z, Gandomi K, Sekhar S C, Pilitsis J, Nycz C, Fischer G. NeuroPlan: A surgical planning toolkit for an MRI-compatible stereotactic neurosurgery robot. International Symposium on Medical Robotics (ISMR). 2021.
241. Lee SL, Chung A, Lerotic M, Hawkins MA, Tait D, Yang GZ. Dynamic shape instantiation for intra-operative guidance. Med Image Comput Comput Assist Interv. 2010;13(Pt 1):69–76 Lecture Notes in Computer Science (including subseries Lecture Notes in Artificial Intelligence and Lecture Notes in Bioinformatics).
242. Zhou XY, Yang GZ, Lee SL. A real-time and registration-free framework for dynamic shape instantiation. Med Image Anal. 2018;44:86–97.
243. Mehrtash A, Ghafoorian M, Pernelle G, Ziaei A, Heslinga FG, Tuncali K, Fedorov A, Kikinis R, Tempany CM, Wells WM, Abolmaesumi P, Kapur T. Automatic needle segmentation and localization in MRI With 3-D convolutional neural networks: application to MRI-targeted prostate biopsy. IEEE Trans Med Imaging. 2019;38(4):1026–36.
244. Li XZ, Young AS, Raman SS, Lu DS, Lee YH, Tsao TC, Wu HH. Automatic needle tracking using Mask R-CNN for MRI-guided percutaneous interventions. Int J Comput Ass Rad. 2020;15(10):1673–84.
245. Lee YH, Li XZ, Simonelli J, Lu D, Wu HH, Tsao TC. Adaptive tracking control of one-dimensional respiration induced moving targets by real-time magnetic resonance imaging feedback. IEEE ASME Trans Mechatron. 2020;25(4):1894–903.
246. Sutherland GR, Lama S, Gan LS, Wolfsberger S, Zareinia K. Merging machines with microsurgery: clinical experience with neuroArm: clinical article. J Neurosurg. 2013;118(3):521–9.
247. Bock M, Krafft A, Maier F, Umathum R, Homagk A-K, Alt S, Zhang K, Pitsaer C, Jenne J, Semmler W. Robotic Systems for MR-Guided Interventions. IFMBE Proceedings. 2009.
248. Kholmovski EG, Coulombe N, Silvernagel J, Angel N, Parker D, Macleod R, Marrouche N, Ranjan R. Real-Time MRI-Guided Cardiac Cryo-Ablation: A Feasibility Study. 2016;27(5):602–8.
249. Golestanirad L, Kirsch J, Bonmassar G, Downs S, Elahi B, Martin A, Iacono M-I, Angelone LM, Keil B, Wald LL, Pilitsis J. RF-induced heating in tissue near bilateral DBS implants during MRI at 1.5 T and 3T: The role of surgical lead management. Neuroimage. 2019;184:566–76.
250. Manan AA, Yahya N, Idris Z, Manan HA. The utilization of diffusion tensor imaging as an image-guided tool in brain tumor resection surgery: a systematic review. Cancers. 2022;14(10):2466.
251. Wei HJ, Zhang CC, Wang T, He NY, Li DY, Zhang YY, Liu CL, Yan FH, Sun BM. Precise targeting of the globus pallidus internus with quantitative susceptibility mapping for deep brain stimulation surgery. J Neurosurg. 2020;133(5):1605–11.
252. Silva MA, See AP, Essayed WI, Golby AJ, Tie YM. Challenges and techniques for presurgical brain mapping with functional MRI. Neuroimage-Clin. 2018;17:794–803.
253. Di Ieva A, Grizzi F, Rognone E, Tse ZTH, Parittotokkaporn T, Rodriguez y Baena F, Tschabitscher M, Matula C, Trattnig S, Baena RRY. Magnetic resonance elastography: a general overview of its current and future applications in brain imaging. Neurosurg Rev. 2010;33(2):137–45.
254. Snyder J, Noujaim D, Mikkelsen T. Chapter 31 - Magnetic resonance spectroscopy. In: Newton HB, editor. Handbook of Neuro-Oncology Neuroimaging (Third Edition): Academic Press; 2022. p. 385–94.

255. Peschke E, Ulloa P, Jansen O, Hoevener JB. Metallic implants in MRI - hazards and imaging artifacts. Rofo-Fortschr Rontg. 2021;193(11):1285–93.
256. Yang G-Z, Cambias J, Cleary K, Daimler E, Drake J, Dupont PE, Hata N, Kazanzides P, Martel S, Patel RV. Medical robotics—regulatory, ethical, and legal considerations for increasing levels of autonomy. Sci Robot. 2017;2(4):8638.
257. Wald LL, McDaniel PC, Witzel T, Stockmann JP, Cooley CZ. Low-cost and portable MRI. J Magn Reson Imaging. 2020;52(3):686–96.
258. Liu YL, Leong ATL, Zhao YJ, Xiao LF, Mak HKF, Tsang ACO, Lau GKK, Leung GKK, Wu EX. A low-cost and shielding-free ultra-low-field brain MRI scanner. Nat Commun. 2021;12(1):7238.
259. Arnold TC, Freeman CW, Litt B, Stein JM. Low-field MRI: clinical promise and challenges. J Magn Reson Imaging. 2023;57(1):25–44.